

# Asteroid Models from Multiple Data Sources

**Josef Ďurech**

Astronomical Institute, Faculty of Mathematics and Physics, Charles University in Prague

**Benoît Carry**

Institut de Mécanique Céleste et de Calcul des Éphémérides

**Marco Delbo**

Laboratoire Lagrange, UNS-CNRS-Observatoire de la Côte d’Azur

**Mikko Kaasalainen**

Tampere University of Technology

**Matti Viikinkoski**

Tampere University of Technology

In the past decade, hundreds of asteroid shape models have been derived using the lightcurve inversion method. At the same time, a new framework of 3-D shape modeling based on the combined analysis of widely different data sources such as optical lightcurves, disk-resolved images, stellar occultation timings, mid-infrared thermal radiometry, optical interferometry, and radar delay-Doppler data, has been developed. This multi-data approach allows the determination of most of the physical and surface properties of asteroids in a single, coherent inversion, with spectacular results. We review the main results of asteroid lightcurve inversion and also recent advances in multi-data modeling. We show that models based on remote sensing data were confirmed by spacecraft encounters with asteroids, and we discuss how the multiplication of highly detailed 3-D models will help to refine our general knowledge of the asteroid population. The physical and surface properties of asteroids, i.e., their spin, 3-D shape, density, thermal inertia, surface roughness, are among the least known of all asteroid properties. Apart for the albedo and diameter, we have access to the whole picture for only a few hundreds of asteroids. These quantities are nevertheless very important to understand as they affect the non-gravitational Yarkovsky effect responsible for meteorite delivery to Earth, or the bulk composition and internal structure of asteroids.

## 1. INTRODUCTION

The determination of asteroid physical properties is an essential part of the complex process of revealing the nature of the asteroid population. In many cases, this process starts with obtaining observational data, continues with creating a model of the asteroid (i.e., its size, 3-D shape, and spin state, in the first approximation), and ends with interpreting new facts based on the model or a set of these. In this sense, modeling is a crucial mid-step between observations and theory. Results based on individual well-studied asteroids can be generalized to other members of the population. On the other hand, a statistically large sample of asteroids with known properties can reveal physical effects that play an important role for the whole population.

In this chapter, we will build on the content of the *Asteroids III* chapter by Kaasalainen *et al.* (2002a) about asteroid models reconstructed from *disk-integrated* photometry. Although visual photometry still remains the most impor-

tant data source of the modeling, the main progress in this field since *Asteroids III* has been the addition of *complementary data sources*. Many of these data sources are *disk-resolved*, thus containing much more information than disk-integrated data. This shift in paradigm – using photometry not alone but simultaneously with complementary data – was mentioned in the last paragraph of the *Asteroids III* chapter as “*perhaps the most interesting future prospect*”, and we are now at this stage. In the following, we will review all data types suitable for inversion, their sources, uncertainties, and how they can be used in modeling.

When describing the methods of data inversion and the results obtained by these methods, it is also important to emphasize caveats, ambiguities, and possible sources of errors. Although the description of what can be obtained from different data sources is exciting, the knowledge of what cannot, i.e., what are limitations of our data sets, is of the same importance. Omitting this may lead to over interpretation of results.

This chapter is structured as follows. First we review the main principles of the multimodal inverse problem in Sect. 2. Then, in Sect. 3, we discuss each data type and their contribution to model characteristics and details, and we describe some extensions of the predominant model. In Sect. 4, we discuss the main results based on lightcurve inversion and multimodal asteroid reconstruction. We conclude with prospects for the future in Sect. 5.

## 2. THEORETICAL ASPECTS OF INVERSION AND DATA FUSION

Asteroid physical model reconstruction from multimodal data is, by its nature, a mathematical inverse problem. It is ill-posed; i.e., the uniqueness and stability properties of the solution are usually not very good unless the data are supported by a number of prior constraints. Furthermore, it is not sufficient just to fit some model to the data numerically and try to probe the solution space with some scheme. Although there are more approaches to the problem of asteroid shape reconstruction, they are usually dealing with only one data type and we mention them in the next section. Here, we describe the problem in a general way in the framework of *generalized projections*: our data are various 1-D or 2-D projection types of a 3-D model, and understanding the fundamental mathematical properties of the inverse projection mapping is essential. This includes a number of theorems on uniqueness, information content, and stability properties (Kaasalainen and Lamberg, 2006; Kaasalainen, 2011; Viikinkoski and Kaasalainen, 2014).

Let the projection point  $\xi_0$  in the image plane (plane-of-sky or range-Doppler) of the point  $\mathbf{x}_0$  on the body be mapped by the matrix  $A$ :  $\xi_0 = A\mathbf{x}_0$ . Define the set  $\mathcal{I}(\xi)$  for any  $\xi$  as

$$\mathcal{I}(\xi) = \{\mathbf{x} | g(\xi, \mathbf{x}; R, t) h(\mathbf{x}; M, R, t) = 1\}, \quad (1)$$

where we have explicitly shown the time  $t$  and the adjustable parameters:  $M$  for the shape and  $R$  for the rotation. The projection point function  $g(\xi, \mathbf{x}) = 1$  if  $A(R, t)\mathbf{x} = \xi$ , and  $g = 0$  otherwise. The ray-tracing function  $h = 1$  if  $\mathbf{x}$  is visible (for occultation, thermal, and radar data), or visible and illuminated (for disk-resolved imaging and photometry in the optical); otherwise  $h = 0$ . The set  $\mathcal{I}(\xi)$  is numerable and finite. The number of elements in  $\mathcal{I}(\xi)$  is at most one for plane-of-sky projections (each point on the projection corresponds to at most one point of the asteroid's surface); for range-Doppler, it can be more (more points on asteroid's surface can have the same distance to the observer and the same relative radial velocity). Generalized projections, i.e., all the data modes presented in Sect. 3, can now be presented as scalar values  $p(\xi)$  in the image field  $\Omega$ :

$$p(\xi; t) = \int_{\Omega} f(\xi, \eta) \sum_{\mathbf{x} \in \mathcal{I}(\eta)} S(\mathbf{x}; M, R, L, t) d\eta, \quad (2)$$

where  $L$  denotes the luminosity parameters (for scattering or thermal properties), and the luminosity function is denoted by  $S$ . The function  $f$  is the point-spread, pixellation,

or other transfer function of the image field. For interferometry, it is typically the Fourier transform kernel. In fact, the reconstruction process works efficiently by taking the Fourier transform of any image type rather than using the original pixels (Viikinkoski and Kaasalainen, 2014). For lightcurves,  $f = 1$  (and  $\xi$  is irrelevant,  $p(\xi)$  is constant). The surface albedo is usually assumed to be constant, although its variegation can be included in  $S$  by the parameters  $L$  if there are high-quality disk-resolved data. In the case of lightcurves only, we can get an indication of non-uniform albedo and compensate for this with a (non-unique) spot model (Kaasalainen et al., 2001).

The multimodal inverse problem can be expressed as follows. Let us choose as goodness-of-fit measures some functions  $\delta_i$ ,  $i = 1, \dots, n$ , of  $n$  data modalities. Typically,  $\delta$  is the usual  $\chi^2$ -fit form between  $p_{\text{model}}$  and  $p_{\text{obs}}$ . Our task is to construct a joint  $\delta_{\text{tot}}$  with weighting for each data mode:

$$\delta_{\text{tot}}(P, D) = \delta_1(P, D_1) + \sum_{i=2}^n \lambda_{i-1} \delta_i(P, D_i), \quad D = \{D_i\}, \quad (3)$$

where  $D_i$  denotes the data from the source  $i$ ,  $\lambda_{i-1}$  is the weight of the source  $i$ , and  $P = \{M, R, L\}$  is the set of model parameter values. The best-fit result is obtained by minimizing  $\delta_{\text{tot}}$  with nonlinear techniques, typically Levenberg-Marquardt for efficient convergence. Regularization functions  $r(P)$  can be added to the sum; these constrain, for instance, the smoothness of the surface to suppress large variations at small scales, the deviation from principal-axis rotation to force the model to rotate around the shortest inertia axis (assuming uniform density), or the gravitational slope, etc. (Kaasalainen and Viikinkoski, 2012).

The modality (and regularization) weights  $\lambda_i$  are determined using the maximum compatibility estimate (MCE) principle (Kaasalainen, 2011; Kaasalainen and Viikinkoski, 2012). This yields well-defined unique values that are, in essence, the best compromise between the different data sets that often tend to draw the solution in different directions. Moreover, MCE values of weighting parameters are objective, not dependent on users choice, although their values are usually close to those determined subjectively based on experience. Plotting various choices of weights typically results in an L-shaped curve shown in Fig. 1; the best solution is at the corner of the curve. In this way, the reconstruction from complementary data sources is possible even if no single data mode is sufficient for modeling alone.

For practical computations, the surface is rendered as a polyhedron, and  $S$  and  $h$  are computed accordingly with ray-tracing (Kaasalainen et al., 2001). Rather than using each vertex as a free parameter, the surface can be represented in a more compact form with spherical harmonics series (for starlike or octantoid; i.e., generalized starlike, shapes) or subdivision control points (Kaasalainen and Viikinkoski, 2012; Viikinkoski et al., 2015). These *shape supports* are essential for convergence: they

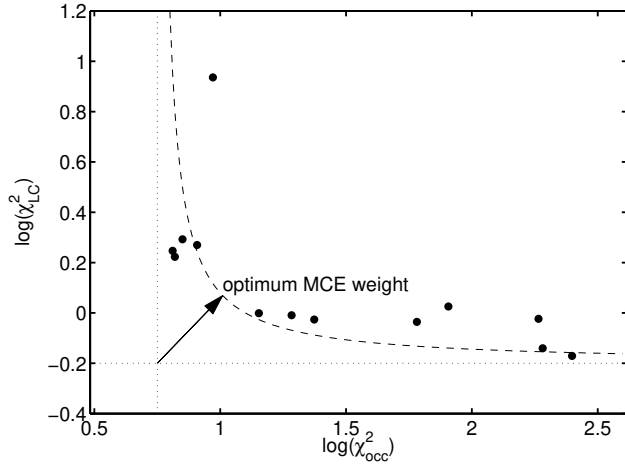


Fig. 1.— The level of fit for lightcurves and occultation data for different weighting between the two data types. The optimum weight is around the “corner” of the L-curve. Each dot corresponds to an inversion with a different weight  $\lambda$ .

allow flexible modifications of the surface with a moderate number of parameters while not getting stuck in local minima or over-emphasizing the role of regularization functions when searching for the best-fit solution. Each shape support has its own characteristic way of representing global and local features. For example, the octantoid parametrization

$$\mathbf{x}(\theta, \varphi) = \begin{cases} x(\theta, \varphi) = e^{a(\theta, \varphi)} \sin \theta \cos \varphi, \\ y(\theta, \varphi) = e^{a(\theta, \varphi) + b(\theta, \varphi)} \sin \theta \sin \varphi, \\ z(\theta, \varphi) = e^{a(\theta, \varphi) + c(\theta, \varphi)} \cos \theta, \end{cases} \quad (4)$$

where  $a$ ,  $b$ , and  $c$  are linear combinations of the (real) spherical harmonic functions  $Y_l^m(\theta, \varphi)$ , with coefficients  $\{a_{lm}\}$ ,  $\{b_{lm}\}$ , and  $\{c_{lm}\}$ , respectively, is easy to regularize globally while retaining the ability to produce local details. The coordinates  $(\theta, \varphi)$ ,  $0 \leq \theta \leq \pi$ ,  $0 \leq \varphi < 2\pi$ , parametrize the surface on the unit sphere  $S^2$  but do not represent any physical directions such as polar coordinates.

This inverse problem is a typical example of a case where model and systematic errors dominate over random measurement errors. Thus the stability and error estimation of the solution are best examined by using different model types (Fig. 2). In the case of shape, for example, the reliability of the features on the solution can be checked by comparing the results obtained with two or more shape supports (starlike, octantoid, subdivision; Viikinkoski *et al.*, 2015). This yields better estimates than, e.g., Markov chain Monte Carlo sequences that only investigate random error effects within a single model type.

A particular feature of the model reconstruction from disk-resolved data is that the result is dominated by the target image boundaries rather than the pixel brightness distribution within the target image. This is because the information is contained in the pixel contrast which is the largest on the boundary (occultations are special

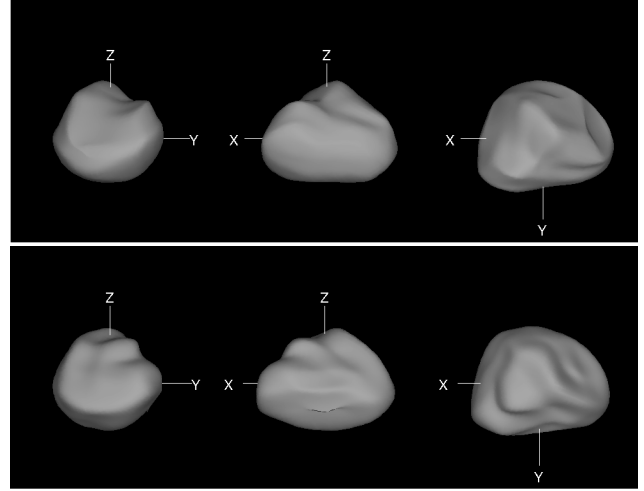


Fig. 2.— Model of (41) Daphne reconstructed from lightcurves and adaptive-optics images using subdivision surfaces (top) and octantoids (bottom). The general shape remains stable, even if small-scale features slightly change.

cases of this as they are samples of the boundary contour). This is very advantageous when considering the effect of model errors in luminosity properties (scattering or thermal models): it is sufficient to have a reasonable model, and the result is not sensitive to the parameters  $L$ . Thus, for example, Atacama Large Millimeter Array data can be used for efficient reconstruction even with a very approximate semianalytical Fourier-series thermal model – more detailed models have hardly any effect on the shape solution (Sect. 3.5, Viikinkoski and Kaasalainen, 2014; Viikinkoski *et al.*, 2015).

### 3. DATA AND MODELING

We describe all data types that can be used, the way of collecting the data, their accuracy, typical number of asteroids for which the data exist, and expectations for the future. We also discuss a typical result of inversion – what is the resolution of the model and how many targets can be modeled (Table 1).

#### 3.1. Photometry

Disk-integrated photometry is, and will always be, the most abundant source of data, because it is available for essentially every single known asteroid. Because asteroid brightness periodically changes with its rotation, frequency analysis of asteroid lightcurves provides asteroid rotation periods – the basic physical property derivable from time-resolved photometry. The regularly updated Asteroid Lightcurve Database of Warner *et al.* (2009) available at <http://www.minorplanet.info/lightcurvedatabase.html> now contains rotation periods and other physical parameters for almost 7000 objects, for about half of them their rotation period is secure and unambiguous. The role of amateur astronomers in this field is traditionally strong, getting even

stronger with increasing level of their technical and software equipment. Hundreds of asteroid lightcurves are published quarterly in the Minor Planet Bulletin; most of them are then archived in the Asteroid Light Curve Database at the Minor Planet Center site ([http://mpc.cfa.harvard.edu/light\\_curve2/light\\_curve.php](http://mpc.cfa.harvard.edu/light_curve2/light_curve.php)) in the ALCDEF standard (Warner *et al.*, 2011). The efficiency of lightcurve production can be increased by dedicated wide-field photometric surveys (Masiero *et al.*, 2009; Polishook *et al.*, 2012, for example), although the period determination from undersampled lightcurves is often ambiguous (Harris *et al.*, 2012).

For period determination, a single lightcurve covering the full rotation is sufficient. However, a set of such lightcurves observed at different geometries (asteroid illuminated and seen from various directions) is needed to reconstruct the shape and spin state of an asteroid. The *lightcurve inversion* method of Kaasalainen and Torppa (2001); Kaasalainen *et al.* (2001) was already reviewed in *Asteroids III* (Kaasalainen *et al.*, 2002a). Since then, the method has been widely used and hundreds of asteroid models have been derived. They are publicly available at the Database of Asteroid Models from Inversion Techniques (DAMIT, <http://astro.troja.mff.cuni.cz/projects/asteroids3D>). The reliability of the method was proved by comparing its results with independent data such as laboratory asteroid model (Kaasalainen *et al.*, 2005), adaptive-optics images (Marchis *et al.*, 2006), stellar occultations (Durech *et al.*, 2011), or spacecraft images of asteroids (2867) Steins (Keller *et al.*, 2010) and (433) Eros (Kaasalainen *et al.*, 2002a).

From disk-integrated photometry alone, only a global shape without any small-scale details can be derived. Because the reflectivity of the surface is not known, the models are not scaled and the information about the size has to come from complementary data. To avoid over-interpretation and artifacts of the modeling, the shapes are usually represented by a *convex* model. This allows to work not in the obvious radius parameter space but in the Gaussian image space (describing a convex body by the curvature of its surface). This is less intuitive but it makes the inverse problem less vulnerable to errors of data and model because of the Minkowski stability (Lamberg and Kaasalainen, 2001) – even if the areas of individual surface facets may change significantly for slightly different data sets, the global convex shape changes very little.

From the practical point of view, we are interested in finding a *unique solution* of the inverse problem. To guarantee this, observations covering a sufficiently wide range of viewing and illumination geometries are needed. For a typical main-belt asteroid, it means observations during several apparitions. For a close-approaching near-Earth asteroid, several months could be sufficient. For more distant objects, we can in principle observe changing lightcurve amplitude because of changing aspect, this would anyway take many decades. Nevertheless, trans-Neptunian objects (TNOs)

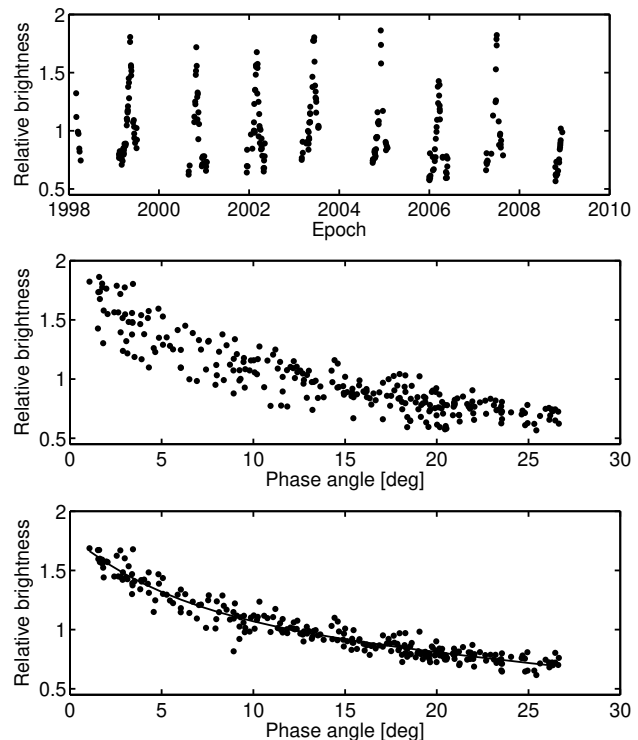


Fig. 3.— Sparse-in-time photometry of (21) Lutetia obtained at US Naval Observatory plotted as a function of time (top) and phase angle (middle). The brightness was reduced to the unit distance from Earth and Sun. The scatter in the phase plot is caused by the intrinsic noise of the data and the rotational and aspect effects. The bottom panel shows residuals for the best-fit model (Fig. 6) plotted over the phase curve (solid curve).

and Centaurs can be never observed from Earth at geometry significantly different from opposition, which is not sufficient to reconstruct a unique convex model (Russell, 1906). If the lightcurves observed in various filters are different, there is some spectral/color variegation over the surface, and a crude color map can be reconstructed (Nathues *et al.*, 2005).

A typical outcome of lightcurve inversion is a convex shape model that describes the global characteristics of the real asteroid. It is also easy to obtain nonconvex versions with the general inversion procedures (see Sect. 2), but then one should produce several solutions with various model types and parameters, and be very cautious about the results (Viikinkoski *et al.*, 2015). In general, disk-integrated photometry contains very little information about nonconvexities unless they are very pronounced or observed at very high phase angles where shadowing effects play an important role (Durech and Kaasalainen, 2003). Nonconvex models seldom fit lightcurves better than convex ones simply because the latter typically already fit the data down to noise level. This sets the resolution limit of photometry (see the discussion in Kaasalainen *et al.*, 2001, 2002a; Viikinkoski *et al.*, 2015, and references therein).

The relative accuracy of the sidereal rotation period de-

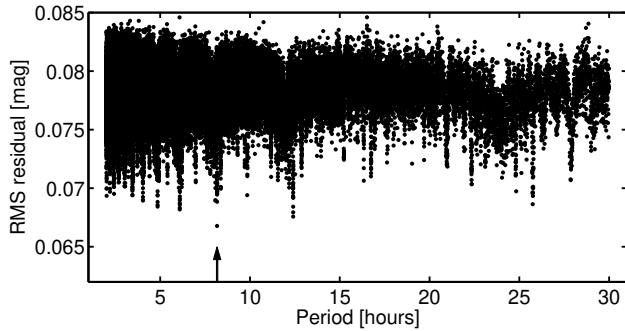


Fig. 4.— Period search for (21) Lutetia. Each point represents a local minimum in the parameter space to which the optimization algorithm converged. The lowest RMS residual (arrow) corresponds to the best-fit model shown in Fig. 6.

terminated from lightcurves is of the order of  $10^{-5}$  or better, depending mainly on the time span of observations. The direction of the spin axis can be determined with an accuracy from a couple of degrees for the models based on many decades of observations with many dense lightcurves, to more than twenty degrees for models based on limited and noisy data. For asteroids orbiting in the ecliptic plane, the geometry for an Earth-based observer is limited to that plane. Then the disk-integrated brightness of a body with surface described by radius vector  $(x, y, z)$  and pole direction  $(\lambda, \beta)$  in ecliptic coordinates is the same as for a body  $(x, y, -z)$  with the spin axis direction  $(\lambda + 180^\circ, \beta)$  (Kaasalainen and Lamberg, 2006). That is why for a typical main-belt asteroid, there are usually two equally good mirror shape solutions with about the same pole latitude and pole longitude difference of about  $180^\circ$ . This ambiguity can be removed with disk-resolved plane-of-sky projections (e.g., images, stellar occultations, see Sect. 3.2, 3.4).

Apart from “classical” lightcurves where the sampling of brightness variations is dense with respect to the rotation period, there are also data that are *sparse in time*. Such data sets typically consist of only a single to a few brightness measurements per night. Provided the whole sparse data set is internally calibrated, it can be used the same way as a standard lightcurve that would be extremely long and very sparsely sampled (Kaasalainen, 2004). These data are routinely provided by all-sky astrometric surveys with various – usually poor – photometric quality. Current surveys provide data of accuracy scarcely better than 0.1 mag. Given a typical lightcurve amplitude of 0.3 mag, the signal is often drowned in noise and systematic errors. This leads to many physically acceptable models fitting the data to the noise level (Ďurech et al., 2005). However, the total amount of data is huge and it has been shown that at least for some asteroids, models can be successfully derived from these data or from their combination with dense lightcurves (Ďurech et al., 2009; Hanuš et al., 2011).

As an example, we show sparse photometry for asteroid (21) Lutetia from US Naval Observatory (260 points covering ten years) in Fig. 3 and the period search results in

Fig. 4. The best-fit model based on this data set has the same rotation period and a similar spin axis direction as the models based on much larger and multiple data sets (Fig. 6).

When using noisy sparse data or only a limited number of data points, a simple shape model of a triaxial ellipsoid is usually sufficient to model the data and to derive the correct period and spin vector orientation (Cellino et al., 2009; Cellino and Dell’Oro, 2012; Carbognani et al., 2012). The advantage of this approach is that the shape is described by only two parameters (axes ratios) and the scanning of the period parameter space is much faster than with general shapes.

The on-going (Pan-STARRS, Catalina, Gaia) and future (ATLAS, LSST) surveys will provide new data every night for essentially every known asteroid. Using this data for automated lightcurve inversion with well-mastered treatment of systematic effects, recognition of the best-fit models, definition of uniqueness of the solution etc., is the main challenge for the future lightcurve inversion.

### 3.2. Remote sensing disk-resolved images

The most direct way to obtain information on the shape of an asteroid is to take pictures of it. The apparent shape as visible on the plane of the sky is delimited by the limb and the terminator, and multiple views obtained while the target rotates can fully characterize its 3-D shape. To resolve the small angular diameter ( $< 0.5''$ ) sustained by asteroids, large facilities are, however, required.

In the 1980s, speckle imaging or speckle interferometry provided “the first glimpses of an asteroid’s surface” (i.e., (4) Vesta by Drummond et al., 1988). This technique is based on the analysis of the speckle pattern in the images of astronomical sources obtained through large telescopes at high magnification power and very short integration time. The aim is to overcome the blurring effects due to the astronomical seeing and to attain diffraction-limited resolution images. Speckle interferometry has been commonly used to study the size, shapes, and surface features of the largest asteroids (Drummond et al., 1985, 1988; Ragazzoni et al., 2000; Cellino et al., 2003). With the launch of the Hubble Space Telescope (HST) in orbit and the first light of the large (10-m class) ground-based telescopes equipped with adaptive-optics fed cameras (e.g., W. M. Keck, European Southern Observatory (ESO) Very Large Telescope (VLT), Gemini, Subaru), the importance of speckle interferometry has decreased.

The critical issue in direct imaging is of course the angular resolution. Any image is the result of the convolution of the object on the plane of the sky with the instrument response, the point spread function (PSF). In space, the PSF is stable and corresponds to the diffraction pattern of the telescope. From the ground, the atmospheric turbulence constantly deforms the PSF and blurs the images, hence the need of real-time correction of the PSF by adaptive optics (AO). The technical challenges of sending a large telescope in space and of building deformable

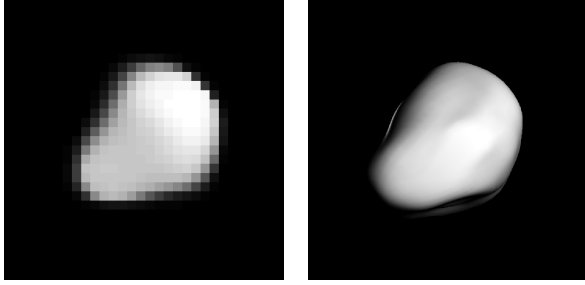


Fig. 5.— Deconvolved adaptive optics image (left) of asteroid (41) Daphne, and the corresponding image of the reconstructed model (right, projection of the octantoid model from Fig. 2). The model is shown under artificial illumination that enhances its 3-D shape and is different from the simple light-scattering model used for the inversion. The AO image has resolution of 10 mas/pixel. The model was reconstructed from 14 AO images obtained with ESO VLT and several lightcurves.

mirrors, explain why the first disk-resolved images in the 1990s were still limited in resolution and only the largest asteroids (1) Ceres, (2) Pallas, and (4) Vesta have been imaged. In the decade since *Asteroids III*, numerous studies have been based on direct imaging of asteroids (e.g., Thomas *et al.*, 2005; Carry *et al.*, 2008; Descamps *et al.*, 2008; Schmidt *et al.*, 2009; Marchis *et al.*, 2013).

Both from space or with adaptive optics on the ground, however, the contrast and angular resolution can be improved by deconvolution of the image by the PSF. This is particularly true for images acquired from the ground with residuals from non-perfect AO correction. Deconvolution is an ill-posed problem, but robust algorithms adapted to planetary images are available (Conan *et al.*, 2000; Mugnier *et al.*, 2004; Hom *et al.*, 2007) and have been validated on sky (Witasse *et al.*, 2006). It is nevertheless the most critical part of the post-processing, as an incorrect deconvolution can introduce a systematic error on the apparent size. An example of an AO image and the reconstructed shape model for asteroid (41) Daphne is shown in Fig. 5

Current facilities deliver an angular resolution of about 30 to 50 milliarcseconds (mas), depending on the wavelength. The apparent shape can therefore be measured for asteroids with an apparent diameter larger than  $\approx 80$ –100 mas, i.e., a couple of hundred targets. Simulations and observations of known targets such as the satellites of Saturn (Marchis *et al.*, 2006; Drummond *et al.*, 2009; Carry, 2009) have shown that a precision of a few mas can be derived on the 2-D profile on the plane of the sky, corresponding to only a few kilometers for main-belt asteroids. With upcoming large telescopes (30+ m, such as the Thirty Meter Telescope or the European Extremely Large Telescope), the angular resolution will be improved by a factor 3–4, providing more than 500 targets. Second generation instruments with extreme AO foreseen on these telescopes should allow the observation of about 7000 asteroids, with sizes of only a few kilometers (Merline *et al.*, 2013).

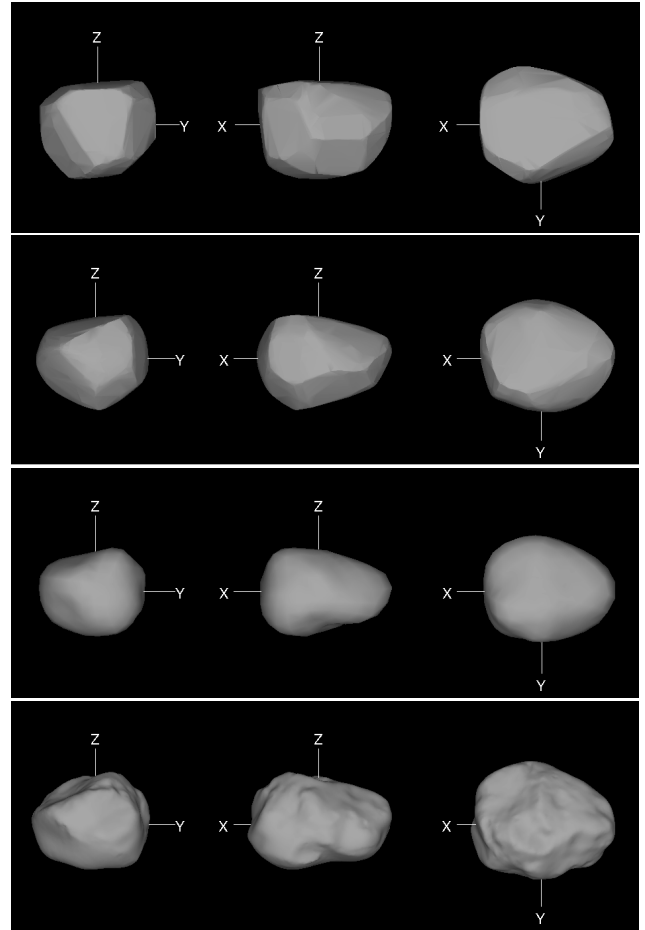


Fig. 6.— Different shape models for (21) Lutetia derived from different sets of data. The level of detail increases with more data from top to bottom: sparse photometry (Sect. 3.1), dense lightcurves (Torppa *et al.*, 2003), lightcurves and AO (Carry *et al.*, 2010b), Rosetta flyby (Sierks *et al.*, 2011).

Using disk-resolved images, giant craters have been discovered (Thomas *et al.*, 1997; Conrad *et al.*, 2007), ambiguity in spin solutions have been solved (Marchis *et al.*, 2006; Carry *et al.*, 2010a), albedo maps have been constructed (Li *et al.*, 2006; Carry *et al.*, 2008), convex 3-D shape models from lightcurves have been set to scale (Hanuš *et al.*, 2013a), and full 3-D shape models determined (Carry *et al.*, 2010b; Descamps *et al.*, 2011).

### 3.3. Flybys

Asteroid imaging and mapping *in situ* is essentially an extreme example of disk-resolved images. The modeling in such cases is more a cartographic than an inverse problem as the data are abundant, directly usable (containing identification points on the surface, etc.), and high-resolution (there is no ill-posedness). However, asteroid flybys, during which roughly a half of the target is likely to remain unseen (not visible and illuminated), pose a special problem: how to see the dark side? The principle here is to use the high-resolution map of the seen side,

constructed with a number of methods of photoclinometry, photogrammetry, and image fitting (Preusker et al., 2012; Gaskell et al., 2008; Jorda et al., 2012), as a constraint in the otherwise same multi-mode inverse problem as with ground-based observations. The procedure is described in Kaasalainen and Viikinkoski (2012); with it, the reconstruction of the dark side, such as those of (2867) Šteins (Keller et al., 2010) or (21) Lutetia (Sierks et al., 2011, see also Fig. 6), is more detailed than from, e.g., lightcurves alone. This is because half of the target is accurately reconstructed, with practically no error margin: therefore the fluctuation margin of the dark side is considerably smaller as well.

### 3.4. Stellar occultations

The observation of a stellar occultation consists in recording the duration of the disappearance of a star behind the asteroid. Knowing the apparent motion of the asteroid on the plane of the sky, obtained from its ephemeris, this duration can be converted in a physical length on the disk of the asteroid, called a chord. Provided several observers record the same event from different locations on Earth, the 2-D profile of the asteroid is drawn on the plane of the sky (Millis and Dunham, 1989). The main difference with disk-resolved imaging resides in the profile, made by only the limb for occultations, and limb+terminator for imaging. In fine, both techniques provide the 2-D profile of the target as projected on the plane of the sky at the epoch of observations (Fig. 7).

Disk-resolved imaging and stellar occultation are, however, radically different in term of facilities, data processing, potential targets, reproducibility, and achievable precision. For stellar occultations, the properties of the occulted star matter generally more than the actual target: the asteroid. If the occulted star is bright enough, its occultation, even by a very small asteroid, can be detected with small aperture telescopes. This is of course the main advantage of stellar occultations, where the apparent size and shape of potentially any asteroid can be measured. Moreover, this technique can be successfully used also for distant TNOs, which have angular sizes too small to be resolved by imaging (Sicardy et al., 2011). In practice, however, a given asteroid will only seldom occult bright stars. Measurements are thus hard, if not impossible, to reproduce.

Stellar occultations are nevertheless extremely valuable. The accuracy of the timing is dictated by time-series photometry, and can therefore be extremely precise. An uncertainty of 50 ms in timings converts into only a 300 m uncertainty in the length of the chord, typical for a main-belt asteroid (at 1.5 au from Earth with an apparent motion of  $10''/\text{h}$ ). The main source of uncertainty is, however, the absolute timing of each chord, required to align them on the plane of the sky. Most of historical occultations were recorded by naked eye, and suffered from this. Since a decade ago, thanks to the availability of low-cost positioning and timing systems (e.g., GPS), stellar occultations are

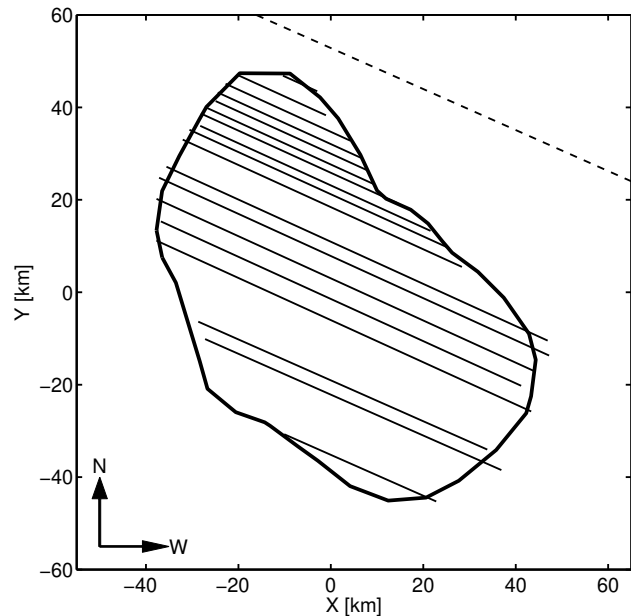


Fig. 7.— An example of a well-covered occultation that provides almost an “image” of the projected asteroid (135) Hertha (Timerson et al., 2009). The model of Hertha based on its lightcurves and occultation data is over plotted. The dashed line is a negative observation constraining the northern part of the model’s projection. Formal timing uncertainties are between 0.02 and 0.2 s, corresponding to 0.12–1.2 km in the projection, which is below the resolution of the model. The RMS of the fit is 1.9 km.

being more and more valuable.

The main contributors to the field are currently amateur astronomers: for a given event, observers have to move to set themselves on the predicted occultation path on Earth. Small aperture ( $< 20$  cm) mobile stations are therefore ideal for recording stellar occultations. Because of the uncertainties of the star and asteroid positions on sky, there is generally an uncertainty of a few tens of kilometers in the location of the occultation path on Earth, requiring observers to spread over large area to cover the event. This usually prohibits dense coverage of the asteroid profile. When only a couple of chords are available, the event provides only limited information on the size, if any on the shape. Current occultation predictions of sufficient accuracy concern only stars in the Hipparcos catalogue and large (at least tens of kilometers) asteroids. With the upcoming publication of the ESA Gaia stellar catalog, and update of asteroid orbits, this position uncertainty is expected to drop significantly and future occultations will be easier to predict, hence observe (Tanga and Delbo, 2007).

Overall, stellar occultations can provide precise measurements of the size and shape of an asteroid, as projected on the plane of the sky. However, events are rare for a given target. Occultations are therefore very valuable in combined data sets, as for instance, to set scale to otherwise dimensionless 3-D shape models (e.g., Āurech et al., 2011; Hanuš et al., 2011). From almost 2500 occultations com-

piled by *Dunham et al.* (2014), there are about 160 “good” ones that allow a reliable determination of asteroid’s size and about 40 “excellent” ones that show details in asteroid’s profile.

### 3.5. Interferometry

Another technique to overcome the limitations of small angular sizes of asteroids, in order to measure their sizes, shapes, and possible presence of satellites, is interferometry. An astronomical interferometer combines coherently (i.e., conserving the phase information) the light from two or more apertures of the same telescope or of distinct telescopes spaced by a distance  $B$ . The spatial resolution (in radians) is of the order of  $\lambda/B$  where  $\lambda$  is the wavelength.

In the following, we give a basic introduction to interferometry of asteroids. Further details can be found in the following works: *Jankov* (2010) and *Matter et al.* (2013) for a broad introduction to astronomical optical interferometry, methods and instrumentation; *Delbo et al.* (2009) for a description of the techniques, and the models for deriving the size and basic shape proprieties of asteroids from the ESO Very Large Telescope Interferometer (VLTI) MIDI-infrared Interferometric instrument (MIDI) data; *Carry et al.* (2015) for an extension of the technique of *Delbo et al.* (2009) to the determination of the sizes and the separation of binary asteroids; *Matter et al.* (2011) for a description and the extension of a thermophysical model to the analysis of interferometric data of asteroids with the aim of obtaining surface properties such as the thermal inertia.

Interferometers measure the coherence function of the source, also called the interferometric visibility, which is given by the ratio between the correlated and the total flux. The correlated flux is the amount of flux in the interferometric fringes. More precisely the correlated flux is the Fourier transform of the brightness distribution of the source measured on the interferometer’s baseline projected on the plane of the sky (see *Delbo et al.*, 2009, for example, and references therein).

The Fine Guidance Sensors (FGS) aboard the Hubble Space Telescope (HST) are optical white-light shearing interferometers (*Nelan et al.*, 1998) that combine the light from distinct apertures of the HST primary mirror and have been used to measure the size and basic shape properties of asteroids (*Hestroffer et al.*, 2002; *Tanga et al.*, 2003). HST/FGS data have clearly demonstrated the bi-lobed nature of some bodies such as (216) Kleopatra (*Tanga et al.*, 2001) and (624) Hektor (*Tanga et al.*, 2003), but were not able to detect the presence of the little moons orbiting these asteroids (*Descamps et al.*, 2011; *Marchis et al.*, 2014), due to the large magnitude difference between the asteroids and their respective moons. Despite the impressive angular resolution of a few mas, corresponding to a few kilometers at a distance of 1.2–1.5 au, a clear limitation of HST/FGS asteroid studies is the bright limiting magnitude of the instrument of about  $V \sim 13\text{--}14\text{ mag}$  (*Tanga et al.*, 2003). A recapitulation of the HST/FGS asteroids results can be

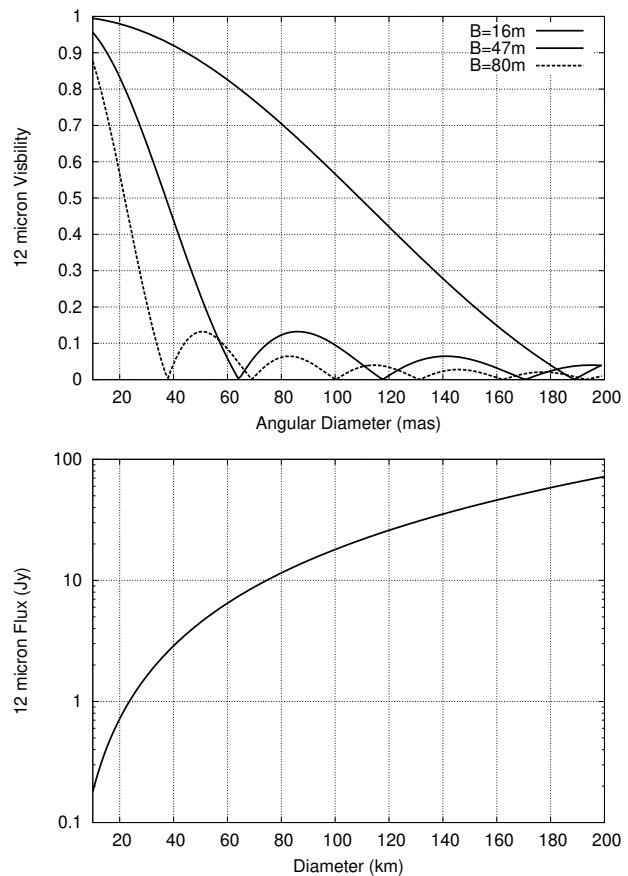


Fig. 8.— Visibility and total flux for an asteroid at 2.5 au from Sun and 1.5 au from Earth as a function of its diameter for different values of the baseline. The MIDI limiting correlated flux (flux times visibility) is 0.5–1 Jy and 10–20 Jy for the UTs and the ATs respectively. Similar limiting fluxes are expected for MATISSE. See text for further details.

found in *Dotto et al.* (2002).

Ground-based interferometry is limited to observation of bright targets because of the requirement to take exposures shorter than the atmospheric coherence time of a few milliseconds. The limiting magnitudes of ground-based long-baseline interferometers and the intrinsic low surface brightness of asteroids, have prevented the use of these instruments for the studies of small solar system bodies until the availability of the VLTI.

Interferometry in the mid-infrared was proven to be also very sensitive to the global shape of asteroids and also to their surface characteristics (*Matter et al.*, 2011, 2013). In particular, since observations are typically carried out in the thermal infrared (8–13  $\mu\text{m}$ ), MIDI data are sensitive to the surface temperature distribution, which is strongly affected by the value of the thermal inertia (*Delbo et al.*, this volume).

Figure 8 shows the visibility and the total flux as a function of the angular diameter of an asteroid at 2.5 au from Sun and at 1.5 au from Earth, where 1 mas roughly corre-

sponds to 1 km on the asteroid. Note that main-belt asteroids smaller than  $\sim 20$  km cannot be easily observed with MIDI at the VLTI. There are about thousand known asteroids with diameter above 20 km, implying that interferometry is potentially an interesting technique for shape modelling. On the other hand, as interferometry in the thermal infrared is sensitive to the spatial distribution of the temperature on the asteroid surface, this technique can be used to determine thermophysical properties of asteroids when the body shapes are known as demonstrated by *Matter et al.* (2011, 2013).

Each VLTI baseline can be used with MIDI only one at the time. MIDI will likely be decommissioned in the near future to be substituted after 2016 by the Multi AperTure mid-Infrared SpectroScopic Experiment (MATISSE). This instrument will combine up to four Unit Telescopes (UTs) or Auxiliary Telescopes (ATs), allowing six simultaneous baselines. This feature will enable us to measure the spatial distribution of the infrared flux along different directions. MATISSE will also measure closure phase relations and thus offer an efficient capability for image reconstruction. In addition to the N band, the MATISSE will also operate in the L and M bands. Unfortunately, MATISSE is not expected to be more sensitive than MIDI.

Another second generation instrument at the VLTI, GRAVITY, that will combine the light from all four UTs, will offer further improvements in spatial resolution compared to MIDI and MATISSE (though with more a more stringent  $V \lesssim 11$  limiting magnitude). It will provide near-infrared adaptive-optics assisted precision narrow-angle (about  $4''$ ) astrometry at the  $10 \mu\text{as}$  level in the K band ( $2.2 \mu\text{m}$ ). Both the reference star and the science object have to lie within the  $\sim 4''$  field of view. In imaging mode, GRAVITY can achieve a resolution of  $\sim 3$  mas in the near-IR (*Eisenhauer et al.*, 2008). The imaging mode can be interesting to precisely measure the sizes and the orbits of the satellites of large asteroids, the latter with  $V \lesssim 11$  mag.

AMBER is the current near-infrared focal instrument of the VLTI. It operates in the J, H, and, K bands (i.e., from  $1.0$  to  $2.4 \mu\text{m}$ ). The AMBER limiting magnitude for asteroid observations is  $V \sim 9$  mag. There is only a handful of asteroids brighter than this limit. These bodies are also the largest ones with angular extensions generally  $> 100$  mas, implying a very low visibility in the J-H-K with the UTs baselines. Although the photometric flux of these few asteroids is such that  $H < 7.5$  mag, their correlated magnitudes due to the low visibilities are much higher than  $7.5$  mag, preventing their fringe detection and tracking in the near-IR.

However, one of the most interesting instruments for asteroid ground based interferometry is the Large Binocular Telescope Interferometer (LBTI). It consists of two  $8.4$ -m telescopes mounted side by side in a single mount, with a  $14.4$ -m center-to-center spacing. This configuration offers a unique capability for interferometry of a Fizeau beam combination. This offers a wide field of view ( $\sim 10$ – $20''$ ) and low thermal background. For example, the LINC-

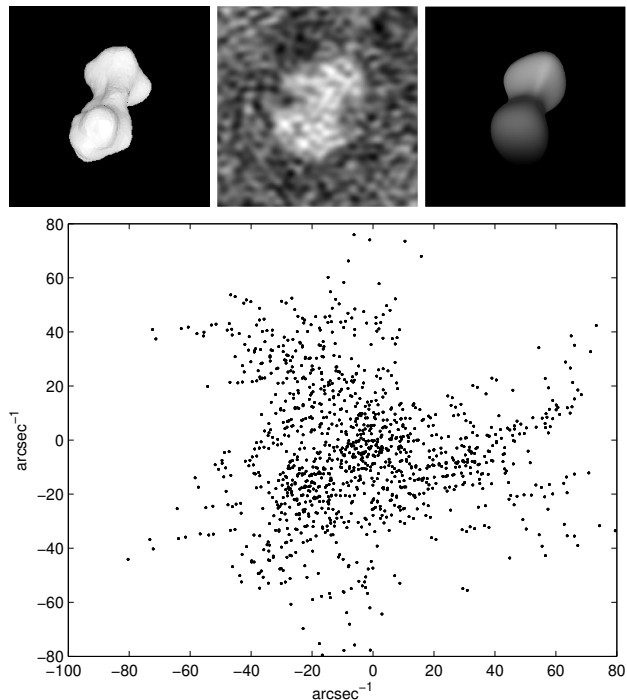


Fig. 9.— Simulated infrared flux from an asteroid (left, a radar shape model of Kleopatra by *Ostro et al.*, 2000) and a “dirty image” (center) with atmospheric noise, obtained by transforming the incompletely sampled frequency plane (bottom, 6000 points, 50 antennas). The smallest resolvable detail is approximately 10 mas. Provided enough observations at different geometries are available (here eight observation runs were used), a shape model (right) can be constructed directly from the raw interferometric data.

NIRVANA instrument can – in principle – be able to resolve binary asteroids whose components are separated  $> 20$  mas. This will allow splitting many binary asteroids.

Another important source of interferometric data in the near future is the Atacama Large Millimeter Array (ALMA). It will provide resolution  $\sim 5$  mas at  $0.3$  mm and a dense mesh of baselines, thus enabling “imaging” of hundreds of asteroids in the main belt (*Busch*, 2009). A useful feature of the multimodal inversion is that the raw ALMA (and any other interferometric) data can be used directly as the original Fourier transform: there is no need to reconstruct the image estimate. What is more, the reconstruction of the overall shape is insensitive to inaccuracies and uncertainties in the thermal model used because the model is determined mainly by the boundary of the projection, the distribution of brightness inside the boundary is much less important (*Viikinkoski and Kaasalainen*, 2014; *Viikinkoski et al.*, 2015). An example of inversion of simulated ALMA data is shown in Fig. 9

Long-baseline interferometry can also represent a novel approach to determine the masses and the densities of asteroids in a range of sizes and distances never studied before. In particular, modern interferometers such as the VLTI, LBTI and the Magdalena Ridge Observatory Interferometer

can spatially resolve binary asteroids discovered by photometric lightcurves in the main belt (*Carry et al.*, 2015). The separation of the components of these systems is too narrow for traditional observational techniques such as AO at 10-m class telescopes.

### 3.6. Direct size measurement with ESA Gaia

The ESA Gaia mission, whose operations started in 2014, will provide accurate astrometry and photometry of asteroids. Photometric data can be used the same way as sparse photometry from ground-based observatories (Sect. 3.1). The potential of Gaia-like data was demonstrated by *Cellino et al.* (2009) on data from the Hipparcos satellite. Apart from disk-integrated brightness, Gaia will provide also direct measurements of asteroid sizes, in a way much similar to the interferometry. Being designed as an astrometry mission at the  $\mu\text{as}$  level, the PSF of Gaia is accurately known and stable. Deviations of the PSF from that of a point-like source can thus be measured and used to estimate the apparent size of asteroids.

Owing to the amount of sources observed by Gaia, the satellite does not download images to Earth, but only 1-D flux profiles, corresponding to small 2-D windows centered on targets, stacked along one direction, similar to interferometry in that respect. Interpretation of this 1-D profile relies therefore on the *a priori* knowledge of the 2-D flux distribution on the plane of the sky. In the creation of Gaia catalog, this will be done iteratively, starting from simple spheres at zero phase angle to finally use the spin and tri-axial ellipsoid solutions determined otherwise from Gaia photometry (*Mignard et al.*, 2007; *Cellino et al.*, 2007).

These measurements represent a great opportunity for multi-data inversion algorithms: the measurement of the extension is direct, but clearly requires a realistic description of the projected shape on the plane of the sky. Considering Gaia specifications and observing geometry, *Mignard et al.* (2007) have estimated the fraction of asteroids for which 1-D dimension will be measured with a precision better than 10%. This fraction is highly dependent on diameter, and 20% of asteroids between 20–30 km will be measured at least once, while all asteroids larger than  $\sim 80$  km will be measured repeatedly.

### 3.7. Disk-integrated radiometry

Measurements of asteroids emission in the thermal infrared – in general at wavelengths between 4–5 and 20–30  $\mu\text{m}$  – are mostly used to determine the sizes of these bodies (*Mainzer et al.*, this volume; *Delbo et al.*, this volume; *Delbo and Harris*, 2002; *Harris and Lagerros*, 2002). Ground based telescopes can only observe in specific windows of the electromagnetic spectrum where the atmosphere is relatively transparent: i.e., the L, M, N, and Q bands at 3, 5, 10, and 20  $\mu\text{m}$ , respectively. However, such observations are strongly affected by the variability of the transparency of the atmosphere and its thermal background. The background also receives contribution from the tele-

scope and the optics. Hence, the thermal infrared observation of asteroids from the ground is limited to relatively bright asteroids ( $V \lesssim 18$  mag with 10-m class telescopes). Absolute calibration of the flux is rarely better than 5–10%. On the other hand, in space the instrument calibration is usually stable and there is no need to reduce the thermal background from the atmosphere. As a consequence, space based telescopes such as Spitzer can observe much fainter and smaller asteroids (*Mommert et al.*, 2014), with uncertainties in the calibration that can reach  $\sim 1\%$  error. Also, from space the range of the observational wavelength is limited only by the detector technology, typically  $\sim 3.5$ –50  $\mu\text{m}$ . At longer wavelengths, the telescope optics require cooling and the observation of faint objects is confronted with the background from solar system dust cloud and infrared cirrus.

In the *Asteroids III* era, the main source of thermal infrared observations of asteroids has been the IRAS Minor Planet Survey that collected observations of more than 2200 asteroids (*Tedesco et al.*, 2002). Since then, the NASA Wide-field Infrared Survey Explorer (WISE) has observed more than 130,000 main-belt asteroids (*Mainzer et al.*, this volume; *Masiero et al.*, 2012, 2011), about 500 near-Earth asteroids (*Mainzer et al.*, 2011, 2012b,a), about 1100 Hilda asteroids (*Grav et al.*, 2012a), and almost 2000 Jupiter-Trojan asteroids (*Grav et al.*, 2012b, 2011) in four infrared wavelengths at 3.4, 4.6, 12, and 22  $\mu\text{m}$ ; the AKARI space telescope observed more than 5000 asteroids during its mission (*Usui et al.*, 2011, 2013; *Hasegawa et al.*, 2013); the Spitzer space telescope observed hundreds of asteroids (e.g., *Emery et al.*, 2006; *Trilling et al.*, 2010; *Licandro et al.*, 2012, among others); the Herschel Space Observatory, that, due to its longer wavelengths, spanning 55–671  $\mu\text{m}$ , was primarily used to observe trans-Neptunian objects (*Müller et al.*, 2010). For a review about all these missions and their results see *Mainzer et al.*, this volume.

The thermal infrared spectrum of asteroids carries information about their size and surface properties, such as the thermal inertia, roughness and emissivity. These properties are typically derived by interpreting thermal infrared data by means of thermal models (*Mainzer et al.*, this volume; *Delbo et al.*, this volume; *Delbo and Harris*, 2002; *Harris and Lagerros*, 2002). The “simple” thermal models that assume a spherical shape, a Lambertian emission of the surface, and a simplified calculation of the surface temperature distribution are used when we lack knowledge of the asteroid global shape, spin vector and rotation period, which is the majority of the cases. Widely used are, for example, the Near-Earth Asteroid Thermal Model (NEATM, *Harris*, 1998; *Delbo and Harris*, 2002; *Harris and Lagerros*, 2002), or the Standard Thermal Model (STM, *Lebofsky et al.*, 1986; *Harris and Lagerros*, 2002; *Delbo and Harris*, 2002).

However, in order to derive the thermal inertia of an asteroid from measurements of its thermal infrared emission, more sophisticated models, called thermophysical models (TPMs), are needed (*Spencer*, 1990; *Spencer et al.*, 1989;

Lagerros, 1996, 1997, 1998; Rozitis and Green, 2011; Mueller, 2007; Delbo, 2004). Such models are used to calculate the temperature distribution over the body's surface as a function of different parameters, including the thermal inertia. In these models, the asteroid shape is usually fixed and is modeled as a mesh of planar facets. The temperature of each facet is determined by numerically solving the one-dimensional heat diffusion equation using assumed values of the thermal inertia, with the boundary condition given by the time-dependent solar energy absorbed at the surface of the facet (see Delbo *et al.*, this volume, for a review). This latter quantity is calculated from the heliocentric distance of the asteroid, the value assumed for the albedo, and the solar incident angle. Macroscopic surface roughness is usually modelled by adding hemispherical section craters of variable opening angle and variable surface density to each facet. Shadowing and multiple reflections of incident solar and thermally emitted radiation inside craters are taken into account as described by Spencer (1990); Emery *et al.* (1998); Rozitis and Green (2011) and Lagerros (1998). Heat conduction is also accounted for within craters (Spencer *et al.*, 1989; Spencer, 1990; Lagerros, 1996; Delbo, 2004). Surface roughness can be adjusted by changing the opening angle of the craters, the density of the crater distribution, or a combination of both (Mueller, 2007). The total observable thermal emission is calculated by summing the contributions from each facet visible to the observer. Model parameters are adjusted until the best agreement with observational data is obtained, i.e., the least-squares residual of the fit is minimized, thereby constraining the physical properties (albedo, size, macroscopic roughness, and thermal inertia) of the asteroid.

From the point of view of multi-data inversion however, the optimization of thermophysical parameters as described above is a two-step process – first, the spin and shape model is derived from one data type (photometry, radar,...), then this model is fixed and used for deriving thermophysical parameters from another data type (thermal infrared). This approach lacks the possibility to weight the two data types with respect to each other. Moreover, the thermophysical parameters can be very sensitive to small modifications of the input shape and spin, so various modifications of the shape should be tested to see how stable the solution is (Hanuš *et al.*, 2015). Ideally, one should model shape and spin parameters together with thermal parameters. This multi-data approach using lightcurves and thermal infrared data simultaneously was successfully tested by Ďurech *et al.* (2012); Ďurech *et al.* (2014) and in principle it can be used also to data that are sparse in time.

### 3.8. Radar

Radar observations that measure the distribution of echo power in time delay and Doppler frequency (so-called range-Doppler or delay-Doppler measurements) are discussed in detail in Ostro *et al.* (2002) and in Benner *et al.* (this volume). The delay-Doppler projection is many-to-

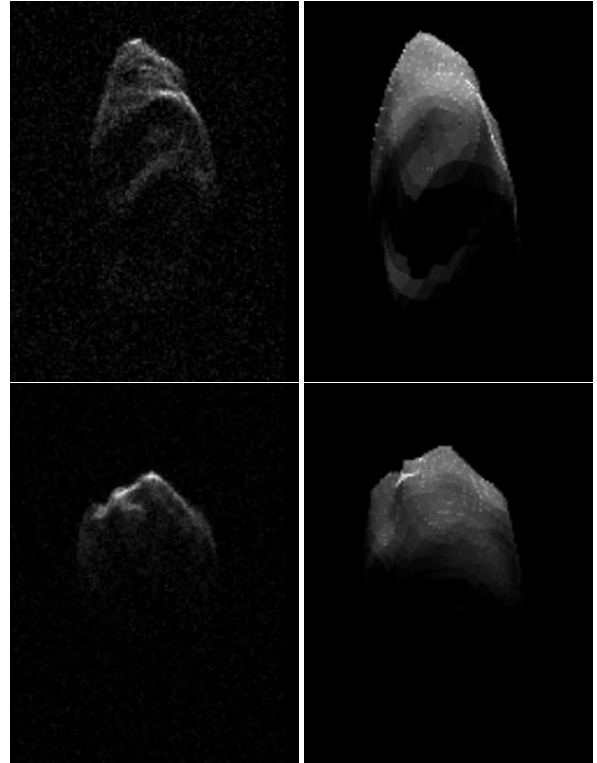


Fig. 10.— Example range-Doppler radar images (left) of asteroid 2000 ET<sub>70</sub> observed at Arecibo observatory (Naidu *et al.*, 2013). Range and frequency resolutions are 15 m and 0.075 Hz, respectively. Range increases towards the bottom, Doppler frequency increases to the right. The simulated images (right) correspond to the reconstructed shape model in Fig. 11.

one mapping of a 3-D surface of the target into a 2-D “image”. Each pixel on the image represents a bin containing integrated echo power from surface elements that have the same distance from the radar and the same relative speed (due to the rotation of the asteroid). From the point of view of inversion, images in the range-Doppler plane are generalized projections that can automatically be handled with the general procedure discussed in Sect. 2 and in detail in Viikinkoski and Kaasalainen (2014) and Viikinkoski *et al.* (2015). In this approach, the multi-mode reconstruction is tuned to produce models with intermediate scale resolution ( $\sim 1/10$  of the diameter) since these are computationally inexpensive (can be obtained in a few minutes with a laptop), and data sources other than radar do not contain more detailed information. An example of radar range-Doppler data of asteroid 2000 ET<sub>70</sub> is shown in Fig. 10 and the corresponding reconstructed shape model in Fig. 11. If detailed radar data are available, such model can then be further refined (Naidu *et al.*, 2013) with the radar techniques described by Benner *et al.* (this volume).

Due to the steep decrease of echo power with the distance to the object (the fourth power of the distance), asteroids achievable by current radar facilities Arecibo and Goldstone are only close-approaching near-Earth asteroids or the largest members of the main belt. A number of exam-

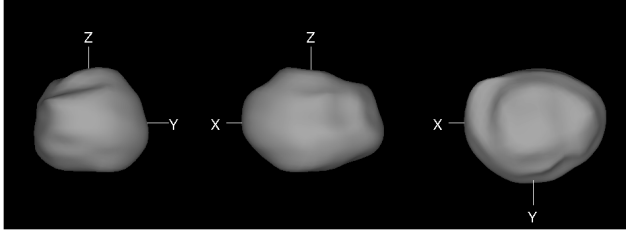


Fig. 11.— Shape model of the asteroid 2000 ET<sub>70</sub> reconstructed from Arecibo and Goldstone delay-Doppler radar images with ADAM (Sect. 3.11).

ples of what can be reconstructed from radar data is given by *Benner et al.* (this volume).

### 3.9. Asteroid interior

We briefly discuss here the interesting possibility of peer into an asteroid. This is somewhat separate from the remote-sensing framework as the data can only be obtained in situ; on the other hand, such data can be acquired with the future space missions. The most practical option is to plant radio transmitters/receivers on the surface of a kilometer-sized asteroid and measure low-frequency ( $\sim 100$  MHz) signals between these and an orbiter when they pass through the interior of the target.

The most robust observables are simply signal travel-time data (*Pursiainen and Kaasalainen, 2013*). These allow an efficient formulation of the inverse problem via the refraction index and are relatively insensitive to noise and model error. Nevertheless, they suffice to give a coarse-scale picture of the general distribution of permittivity inside the asteroid, as well as the locations and sizes of large anomalies (sudden low- or high-density regions such as voids or heavier minerals). This approach has also been robustly tested in laboratory conditions (*Pursiainen and Kaasalainen, 2014b*). A more refined possibility is to measure changes in the pulse profile, although this is more prone to errors (*Pursiainen and Kaasalainen, 2014a*). The interior of the asteroid is practically impossible to model accurately in three dimension since it is supposed to have a number of cracks, voids, discontinuities etc., all refracting and reflecting the radio waves in complicated ways. Thus a very robust scheme is essential for extracting the available information with stability. Regardless of the data type, one or two transmitters on the surface are not sufficient for a unique solution. A tetrahedral configuration of four transmitters would be ideal, but this places heavy demands on the payload design.

### 3.10. Extension of the model

So far, we assumed that the asteroid can be described as a solid single body with constant spin vector, i.e., rotating along the axis with the maximum moment of inertia with a constant rotation rate. Although this model represents a typical asteroid, there are other configurations that can be also treated with an extension of the simple model.

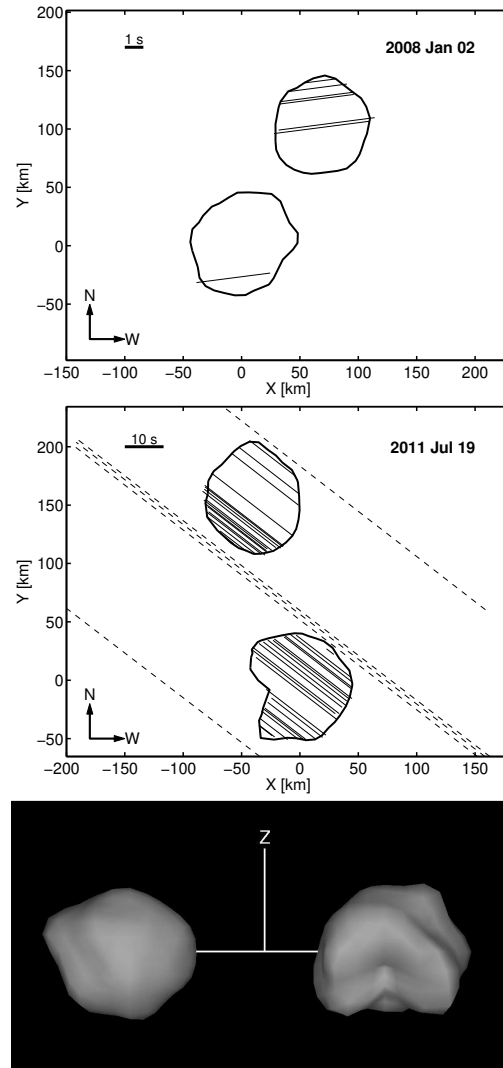


Fig. 12.— Shape model of (90) Antiope seen from its equator (bottom) reconstructed from lightcurves and two occultations observed in 2008 and 2011 (top and middle). The model silhouette is projected on the plane of the sky, the solid lines are positive chords, the dashed ones are negative observations.

#### 3.10.1. Binaries

Binary asteroids form a significant part of the population of small asteroids. *Pravec et al. (2006)* estimated that the fraction of binaries is 15% for the near-Earth population and a similar fraction is assumed for the main-belt population in the same size range (*Margot et al., this volume*). The formation, dynamics, and physical properties of binary and multiple asteroid systems are discussed in detail in other chapters of this volume (*Walsh et al., Margot et al.*). In general, modeling of such systems is more complex because the dynamics has to be taken into account. However, in some cases described below, the technique used for modeling single asteroids can be used also for multiple systems or at least their primary components.

For binary (or multiple) systems where the primary com-

ponent is much larger than the satellite, the photometric signal from the satellite can be neglected and the primary can be modeled as a single body. For such systems, the shape of the primary and the constraints on its gravitational quadrupole  $J_2$  from the orbit analysis of the secondary can be used to investigate the distribution of the density (Berthier *et al.*, 2014; Takahashi and Scheeres, 2014).

For systems with comparable sizes, the problem becomes complicated when the system is asynchronous, i.e., when the rotation period of the primary is different from the orbital period of the secondary. Such systems are usually modeled as two ellipsoids (Scheirich and Pravec, 2009), although more general models were created from radar observation (1999 KW<sub>4</sub>, for example, see Ostro *et al.*, 2006).

Fully synchronous binaries can be approximated by single bodies if the separation of their components is not large. Even a convex model can provide a good fit to the lightcurves (Durech and Kaasalainen, 2003). Such model does not represent the true configuration of the system, of course, but it provides the correct rotation period and direction of the orbital plane.

When the separation of components is larger, the system has to be modeled as two-component. However, from the modeling point of view, it is just a moderate modification of the nonconvex problem, where the system is described by only one rotation/orbital period and orientation of the normal of the orbital plane (parallel to the spins of the bodies). If the model is based on lightcurves only, the spin and period parameters can be reconstructed accurately, but the uncertainty in shapes is large. As has been shown by Marchis *et al.* (2014) on (624) Hektor, the distinction between a highly nonconvex single body, two bodies in contact, or two bodies orbiting each other is difficult to make.

An example of reconstruction of a doubly synchronous binary system (90) Antiope from lightcurves and occultations is shown in Fig. 12, where the model is shown together with the silhouettes from occultations. Tens of chords observed during the occultation in 2011 (Colas *et al.*, 2012) portray the two components to details unattainable by any other observational technique and the large set of lightcurves observed over many apparitions constrains the rotational parameters. A similar model can be obtained also by using lightcurves separately to create a scale-free model that is then scaled by occultation data (the Shaping Asteroids with Genetic Evolution algorithm, Bartczak *et al.*, 2014). However, this two-step approach lacks the advantages of simultaneous inversion where the two data types can be weighted with respect to each other.

### 3.10.2. YORP effect

As described in detail by Vokrouhlický *et al.* (this volume), rotation state of small asteroids is affected by the anisotropic recoil of scattered sunlight and thermal radiation, which causes a net torque called the Yarkovsky-O'Keefe-Radzievskii-Paddack (YORP) effect. This effect secularly changes the obliquity of the spin vector and the

rotation period. Whereas the former is too small to be measured with current data, the latter has been measured on several asteroids (see Table 3 in Vokrouhlický *et al.*, this volume). If the change of the rotation period is larger than the uncertainty of the period, the change can be traced from apparition to apparition as was the case for (54509) YORP (Lowry *et al.*, 2007). In other cases, the effect was much smaller and it revealed itself by the discrepancy between the data and the model assuming the period to be constant (Kaasalainen *et al.*, 2007; Durech *et al.*, 2008, 2012; Lowry *et al.*, 2014).

The YORP effect is easy to include into the model. We assume that the rotation rate  $\omega$  changes linearly in time  $t$  as  $d\omega/dt = v$ . Then the parameter  $v$  is another free parameter of the modeling. Because the shift in the rotation phase increases quadratically in time as  $\phi = \omega t + 1/2 vt^2$ , even small changes  $d\omega/dt$  of the order  $10^{-8}$  rad/d<sup>2</sup> can be detected with data sets covering tens of years.

In principle, the measured value of  $v$  can be compared with the theoretical value computed from the spin state, shape, size, and the thermal parameters of the surface with the density as a free parameter. However, due to sensitivity of YORP on small scale details of the shape that are far below the resolution of the model (Statler, 2009; Kaasalainen and Nortunen, 2013), and the problem of transverse heat diffusion (Golubov and Krugly, 2012; Golubov *et al.*, 2014; Ševeček *et al.*, 2015), this can hardly be more than a rough comparison.

Because the YORP effect scales as inverse of the square of the size of asteroid, it becomes more important for small bodies, where it might be necessary to include it into the modeling if the data cover a wider span of time. YORP is assumed to play an important role in many dynamical processes – the distribution of rotation periods and spin obliquities of small asteroids (Pravec *et al.*, 2008; Hanuš *et al.*, 2013b) or the creation of asteroid binaries and asteroid pairs (Pravec *et al.*, 2010), for example. It is important to have more asteroids with YORP detection. Better statistics of values of period change will help to constrain theories of YORP evolution of small asteroids.

### 3.10.3. Excited rotation

Asteroids rotating in the relaxed mode are fully described by the spin axis direction, rotation rate, and the initial orientation. However, some asteroids are in an excited rotation state, which can be described as a rotating free top. More parameters are needed to describe this tumbling motion (Kaasalainen, 2001). The reason why some asteroids are in this state can be (i) primordial, (ii) collisional excitation (Henyeh and Pravec, 2013), or (iii) end state of YORP-driven spin down. The approach to the modeling is in principle the same as for asteroids in principal axis rotation, only the orientation for a given time is given by solving differential equations. From lightcurves, models of asteroids 2008 TC<sub>3</sub> (Scheirich *et al.*, 2010) and (99942) Apophis (Pravec *et al.*, 2014) have been derived. A model of aster-

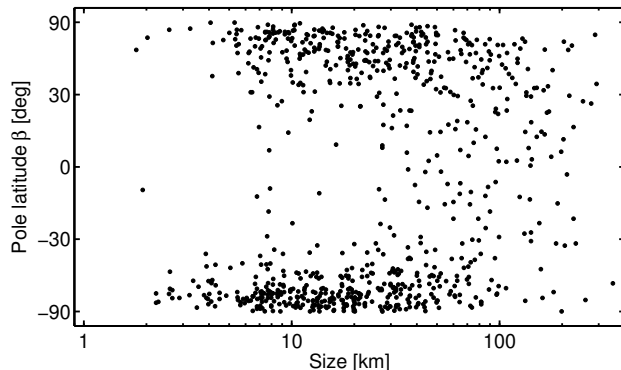


Fig. 13.— Distribution of pole ecliptic latitude  $\beta$  with respect to the size of the asteroid for  $\sim 800$  asteroids. The scale on the vertical axis is linear in  $\sin \beta$ , which makes the vertical distribution of points in this plot uniform for an isotropic distribution of spin vectors.

oid (4179) Toutatis (Hudson *et al.*, 2003) was derived from radar data and lightcurves. This model was later compared with the fly-by images of Chang'E-2 mission – the general shape was in agreement, although there were some minor discrepancies (Zou *et al.*, 2014).

### 3.11. Procedures: Convexinv, KOALA, and ADAM

Software for the inverse problems is available at DAMIT (<http://astro.troja.mff.cuni.cz/projects/asteroids3D>). Convexinv is a procedure for lightcurve inversion, while ADAM (All-Data Asteroid Modeling) is a collection of functions from which one can tailor an inversion procedure for any data sources (Viikinkoski *et al.*, 2015). An earlier version of this is called KOALA (Knitted Occultation, Adaptive optics and Lightcurve Analysis, Carry *et al.*, 2012); this is based on lightcurves and silhouette contours obtainable from images and occultations (Kaasalainen, 2011; Kaasalainen and Viikinkoski, 2012). KOALA is especially suitable for lightcurve and occultation data, while ADAM allows the use of any images (camera, radar, or interferometry) with or without lightcurves without having to process them to extract contours or other information. Both KOALA and ADAM can be used for lightcurves only but, as discussed earlier, this is not reliable. Any resulting shape should only be taken in the global sense (as a more realistic-looking rendering of a convex solution), and the details or nonconvex features are seldom likely to be real (Viikinkoski *et al.*, 2015).

## 4. WHAT HAVE WE LEARNED FROM 3-D SHAPES?

The purpose of modeling methods described in previous sections is to reveal new facts about the nature of asteroids. The approach is made on two fronts: The first strategy is to use the most abundant data sources (photometry in visual and thermal IR) to produce many low-resolution models that will be a statistically significant sample of the whole asteroid population from which conclusions about the phys-

ical properties can be drawn. The second approach is to concentrate on selected targets, obtain as many different data types as possible, create detailed models of these asteroids, and extrapolate the obtained results to the whole class of similar objects. We describe in this section new research areas that directly benefit from availability of spin solutions and 3-D shape models.

### 4.1. Spin-axis distribution and evolution

One of the main results of the lightcurve inversion is the increasing sample of asteroids with known orientation of the spin axis. For main belt asteroids, the long-known lack of asteroids with poles close to the ecliptic (Kryszczyńska *et al.*, 2007) was confirmed and it was shown that it is more pronounced for smaller asteroids (Hanuš *et al.*, 2011). In Fig. 13, we plot the distribution of pole latitudes for  $\sim 800$  asteroid models with respect to their size (an updated version of Fig. 5 in Hanuš *et al.*, 2011). The size-dependent structure can be explained by the YORP effect that is more effective on smaller asteroids ( $\lesssim 30$  km) and pushes them into extreme values of obliquity ( $0^\circ$  or  $180^\circ$ ). This corresponds to the clustering of pole latitudes towards values of  $\pm 90^\circ$ . Although there are observation and modeling biases that affect the distribution of poles in the sample of available models, their effect is only marginal compared to the strong anisotropy seen in Fig. 13 (Hanuš *et al.*, 2011). The spin-axis orientation of even smaller asteroids ( $\lesssim 5$  km) is still not known due to the lack of models. For the largest asteroids ( $\gtrsim 60$  km), there is a statistically significant increase of prograde rotators (98 prograde vs. 63 retrograde in Fig. 13), probably of primordial origin (Johansen and Lacerda, 2010).

A different approach to the problem of spin-axis distribution was used by Bowell *et al.* (2014). They analyzed variations of the mean brightness with the ecliptic longitude, from which they estimated ecliptic longitudes of spin axis for about 350,000 asteroids and revealed a clearly non-uniform distribution. However, the explanation of the cause for this non-uniformity is still missing.

With increasing sample of models, it is also possible to study the distribution of spin axes of members of collisional families. Results of Hanuš *et al.* (2013a) agree with theoretical expectations: if the spread in proper semimajor axis increases with decreasing size due to the Yarkovsky effect (Nesvorný *et al.*, Vokrouhlický *et al.*, this volume), asteroids closer to Sun than the center of the family should rotate retrograde, those farther should rotate prograde. This behavior is shown in Fig. 14 for Flora family.

### 4.2. A pre-requisite in many cases

Unlike most astronomical objects, the viewing geometry of asteroids continuously changes due to their motion relative to observer. As a corollary, knowing their rotation period and spin-vector coordinates is crucial to interpret projected size measurements, and to tie together observations.

As already described in Sect. 3, the spin and 3-D shape

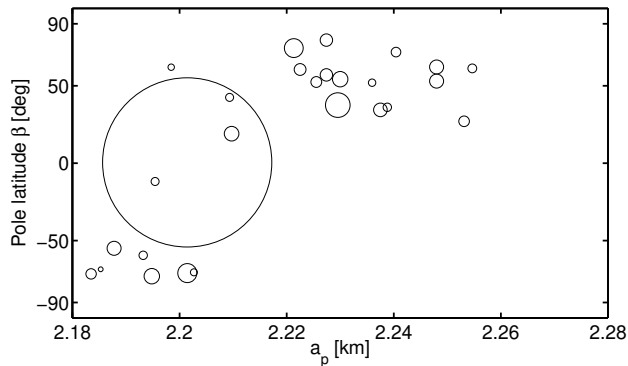


Fig. 14.— Distribution of pole ecliptic latitude  $\beta$  with respect to the proper semimajor axis  $a_p$  of the Flora family members. The relative size of each circle corresponds to the size of the asteroid.

are required to interpret thermal infrared radiometry, stellar occultations, or apparent sizes measured by Gaia without biases. Similarly, there have been long running discussions to explain inconsistent spectral measurements of asteroids, that can be easily solved once the spin properties (period and orientation) are known: see, for instance, the discussion on (832) Karin by *Sasaki et al.* (2004), *Vernazza et al.* (2007), and *Chapman et al.* (2007), or on (21) Lutetia by *Barucci et al.* (2012).

#### 4.3. Density, composition, and internal structure

Density is one of the most fundamental properties to constrain the composition of asteroids and investigate their internal structure (*Scheeres et al.*, this volume). With the exception of binary asteroids with observable mutual eclipses (*Margot et al.*, this volume), both mass and volume are required to determine the density of an asteroid. Estimating the mass of an asteroid by measuring its gravitational influence on other objects is a challenge because of the relative low mass of asteroids compared to other planetary objects. The number of mass determinations thus limits the number of density estimates. Although there are diameter, hence volume, estimates for all asteroids with a mass determination, the uncertainty in volume generally dominates the balance on density uncertainty (*Carry*, 2012).

In this respect, 3-D shape models are required to determine accurate volume. The level of potential biases increases with stronger assumptions on the shape, and accuracy accounting for systematics improves from sphere, to ellipsoid, to convex hull, to the real shape. In the decade since *Asteroids III*, the number of density estimates has increased from 20 to 300 objects (*Britt et al.*, 2002; *Carry*, 2012). Among these, the most reliable are derived from binary systems for which the volume of the primary was determined after shape modeling (e.g., *Ostro et al.*, 2006; *Shepard et al.*, 2006; *Descamps et al.*, 2009, 2011; *Fang et al.*, 2011; *Marchis et al.*, 2013).

A detailed description on the density of asteroids and

their internal structure can be found in *Scheeres et al.* (this volume), from under-dense asteroids, hosting large voids, to over-dense asteroids, likely differentiated. In the context of this chapter, it is important to highlight that not only density estimates more precise than 10–20% can be used to discriminate between different analogue meteorites and can provide insights on the internal structure. Such accuracy can only be achieved with volume known to 5–10% or better, which means that a proper description of the 3-D shape is needed.

#### 4.4. Determination of surface properties by means of TPMs

The spin state and shape model of an asteroid is input information for the TPMs. While in the *Asteroids III* era, shape and spin information were available only for a handful of asteroids, preventing application of TPMs to a large number of these bodies, this situation has drastically changed in the last few years. Physical properties (such as the value of the surface thermal inertia) of about 60 asteroids are now available thanks to the application of TPMs (see *Delbo et al.*, this volume). A remarkable improvement in this field is also represented by the availability of high quality thermal infrared data as those produced by the WISE and the Spitzer space telescopes. In the next few years we expect the number of asteroids with known thermal inertia values to grow thanks to the availability of more shape and spin state models.

#### 4.5. Surface re-arrangement

From the spin, 3-D shape, and density, the local gravity at the surface can be computed. Unsuspected physics has been unveiled with the modeling of the near-Earth asteroid (66391) 1999 KW<sub>4</sub> by *Ostro et al.* (2006). Some small asteroids present an equatorial bulge, presumably generated by regolith migration toward lower gravity regions. This process can even form binary systems if the asteroids spin fast enough (*Walsh et al.*, 2008; *Harris et al.*, 2009).

#### 4.6. Cratering events

An evident outcome of shape modeling is the capability to detect large impact craters and basins. Aside from the spacecraft encounters, the first detection was the large impact basin on Vesta, progenitor of the Vestoids (*Binzel and Xu*, 1993), detected with the HST (*Thomas et al.*, 1997) and confirmed by NASA Dawn spacecraft (*Russell et al.*, 2012). Another case is the recent impact suffered by asteroid (596) Scheila, detected by the presence of a dust tail (*Bodewits et al.*, 2011). Lightcurves obtained before and after the impact, under similar geometries are different, revealing different surface properties (*Bodewits et al.*, 2014).

TABLE 1  
A LIST OF OBSERVATION TECHNIQUES AND DERIVABLE PHYSICAL PROPERTIES.

Technique	Period	Spin	Size	Shape	Thermal Inertia	Number of models		
						Asteroids III	Asteroids IV	Asteroids V
Photometry	X	X		X		30	500	10 <sup>4</sup>
Images		X	X	X		5	50	10 <sup>2</sup>
Occultation		X	X	X		5*	50	10 <sup>2</sup>
Radar	X	X	X	X		10	30	10 <sup>2</sup>
Radiometry			X		X	10*	20	10 <sup>4</sup>
Interferometry		X	X	X		5 <sup>†</sup>	< 10	10 <sup>2</sup>
Fly-by	X	X	X	X	X	6	10	< 15

The “X” mark indicates which physical properties are derivable from which technique. The number of models available at the time of *Asteroids III* book (Asteroids III) and now (Asteroids IV) is only approximate. The Asteroids V column is an order-of-magnitude estimate for the next decade.

\*Ellipsoidal models.

<sup>†</sup>HST/FGS.

#### 4.7. Mass distribution

Because some asteroids are less or more dense than their most-likely constituents, the question of the mass distribution (denser material or voids) in their interior can be asked. This question is intrinsically tied with the study of the gravity field around the asteroid. The latter has been measured during spacecraft encounters (see *Miller et al.*, 2002, for instance), but studies from Earth-bound observations have recently appeared. By comparing the spherical harmonics of the gravity field as determined from the orbit of a natural satellite, with the expected coefficients resulting from the 3-D shape model, the hypothesis of homogeneous mass distribution can be tested (*Vachier et al.*, 2012; *Berthier et al.*, 2014; *Takahashi and Scheeres*, 2014).

#### 5. FUTURE

In the decade since *Asteroids III*, where the principles of lightcurve inversion based on dense-in-time series were presented (*Kaasalainen et al.*, 2002b), the number of models has seen a tenfold increase – from a few tens to a few hundreds (Table 1). The increasing availability of sparse-in-time photometry, and its appropriate handling in the inversion, coupled with a dramatic increase of computer time (thanks to projects like Asteroids@Home) have made this possible. Upcoming all-sky surveys such as Pan-STARRS, LSST, and Gaia are expected to produce enormous data sets and there is little doubt that thousands of models will be derived in the next decade. Our knowledge on non-gravitational effects such as YORP and Yarkovsky will directly benefit from this larger sample.

With the large number of data and models, new challenges will arise – how to extract scientifically interesting information from a large set of models of asteroids? With

big data flows, the processing has to be automated, with effective data processing. The obvious search for correlations has to be done with care because of large biases in the set of models. Although the importance of detailed models of individual well-studied asteroids will be important, the main shift in paradigm and probably the main source of interesting findings will be in tens of thousands of asteroid models derived from photometry in optical and thermal infrared wavelengths. Only a few years ago, only photometry in the visible was available for a large number of asteroids. The situation drastically changed with WISE catalog of thermal fluxes for 150,000 asteroids. Automatized procedures capable of dealing with photometry in the visible and thermal infrared will yield not only 3-D shape and spin state for thousands of asteroids, but also their diameter, albedo, and thermal inertia of their surface. The later being crucial in interpreting asteroid mineralogy once coupled with spectroscopy (*Reddy et al.*, this volume). Understanding of observational and modeling biases will be crucial for correct interpretation of the results. Connecting spin and shape distribution of asteroids with their orbital and spin evolution will hopefully lead to a clear picture of the evolution of the main asteroid belt. The ultimate goal here is the connection of models of evolution of the main belt with spin-axis evolution and current distribution of asteroid physical properties.

Another approach that is complementary to modeling individual objects, is modeling distribution functions of parameters of interest. With any inversion technique and photometric data quality, the number of models will be always much lower than the number of known asteroids just because it takes time to collect enough data at different geometries. So instead of aiming to create unique models for a statistically significant sample of the (sub)populations

with known observational and modeling bias, one can use other observables than the time–brightness pairs. With this approach, there is almost no “wasting” of data because essentially all photometric points are used in the statistical approach. The aim is to model characteristics of a given asteroid population as a whole when there are not enough data to model individual members. One of the observables can be, for example, the mean brightness over one apparition (Bowell *et al.*, 2014) and its dispersion that correlates with lightcurve amplitude. If there are not enough data points to estimate mean brightness and its variance, the statistics of scatter of individual pairs of observations can be used (Szabó and Kiss, 2008). If the data come in pairs of observations separated by a constant time interval (like with Pan-STARRS), the rotation period can be estimated (Durech *et al.*, 2007).

Another challenge for next decade resides in the derivation of a large sample of higher-resolution models, based on multiple data sources. Building inversion techniques capable of handling different data sources had been highlighted in *Asteroids III* as the next step, and this became reality over the past few years. The models based on multiple data sources are more realistic, more reliable, more precise than the independent analysis of individual data sets. If practical issues of merging data sets arise, mathematical solution have been exposed, and algorithms and software are ready and freely available. The current sample of models derived by such methods is nevertheless still limited. If the multi data analysis is more efficient than the independent analysis of the individual data sets, the practical problem of data sharing arises. Although the tools to invert multiple data sources are ready and freely available, the data are still hard to get and harder to share. To maximize the scientific output, it is necessary to combine all available data sources.

The other observing techniques (i.e., disk-resolved imaging, stellar occultations, Gaia size measurements, or radar echoes) will never provide data for more than a few thousands asteroids. The apparent sizes by Gaia will however be measured with a high precision, and will concern a decent sized sample. Because the data will be made public, they should be used on a regular basis for modeling. The number and quality of profiles derived from stellar occultations have always been restricted due to the intrinsic complexity of prediction, and cost of equipment. The parallel availability of low-cost telescopes and cameras, together with the publication of Gaia stellar catalog and asteroid orbits, will open a new age for stellar occultations. Any mass-production procedure of asteroid models should therefore be able to deal not only with photometry (visible and infrared) but also with stellar occultations.

Finally, if the bulk of asteroids are single objects, rotating along their shortest axis, a small fraction will either be in tumbling state, or have satellites. Automatic modeling procedures should be able to detect such cases, triggering detailed analysis of these peculiar targets.

The rising interest of private companies for near-Earth objects as mining resources will inevitably lead to further

development of analysis of remote-sensing data, building dedicated ground-based or space telescopes, and eventually moving from asteroids surface into their interiors.

**Acknowledgments.** The work of JĎ was supported by the grant GACR P209/10/0537 of the Czech Science Foundation. MD acknowledges support from the grant ANR-11-BS56-008 SHOCKS of the French National Research Agency.

## REFERENCES

- Bartczak P., Michałowski T., Santana-Ros T., et al. (2014). A new non-convex model of the binary asteroid 90 Antiope obtained with the SAGE modelling technique. *Mon. Not. R. Astron. Soc.*, 443, 1802–1809.
- Barucci M. A., Belskaya I. N., Fornasier S., et al. (2012). Overview of Lutetia’s surface composition. *Planet. Space Sci.*, 66, 23–30.
- Berthier J., Vachier F., Marchis F., et al. (2014). Physical and dynamical properties of the main belt triple Asteroid (87) Sylvia. *Icarus*, 239, 118–130.
- Binzel R. P. and Xu S. (1993). Chips off of Asteroid 4 Vesta: Evidence for the parent body of basaltic achondrite meteorites. *Science*, 260, 186–191.
- Bodewits D., Kelley M. S., Li J.-Y., et al. (2011). Collisional excavation of asteroid (596) Scheila. *Astrophys. J. Lett.*, 733, L3.
- Bodewits D., Vincent J.-B., and Kelley M. S. P. (2014). Scheila’s scar: Direct evidence of impact surface alteration on a primitive asteroid. *Icarus*, 229, 190–195.
- Bowell E., Oszkiewicz D. A., Wasserman L. H., et al. (2014). Asteroid spin-axis longitudes from the Lowell Observatory database. *Meteoritics and Planetary Science*, 49, 95–102.
- Britt D. T., Yeomans D. K., Housen K. R., et al. (2002). Asteroid Density, Porosity, and Structure. In *Asteroids III* (Bottke W. F., Cellino A., Paolicchi P., et al., editors), pp. 485–500. University of Arizona Press, Tucson.
- Busch M. W. (2009). ALMA and asteroid science. *Icarus*, 200, 347–349.
- Carbognani A., Tanga P., Cellino A., et al. (2012). The representation of asteroid shapes: A test for the inversion of Gaia photometry. *Planet. Space Sci.*, 73, 80–85.
- Carry B. (2009). *Asteroids physical properties from high angular-resolution imaging*. PhD thesis, Observatoire de Paris.
- Carry B. (2012). Density of asteroids. *Planet. Space Sci.*, 73, 98–118.
- Carry B., Dumas C., Fulchignoni M., et al. (2008). Near-infrared mapping and physical properties of the dwarf-planet Ceres. *Astron. Astrophys.*, 478, 235–244.
- Carry B., Dumas C., Kaasalainen M., et al. (2010a). Physical properties of (2) Pallas. *Icarus*, 205, 460–472.
- Carry B., Kaasalainen M., Leyrat C., et al. (2010b). Physical properties of the ESA Rosetta target asteroid (21) Lutetia. II. Shape and flyby geometry. *Astron. Astrophys.*, 523, A94.
- Carry B., Kaasalainen M., Merline W. J., et al. (2012). Shape modeling technique KOALA validated by ESA Rosetta at (21) Lutetia. *Planet. Space Sci.*, 66, 200–212.
- Carry B., Matter A., Scheirich P., et al. (2015). The small binary asteroid (939) Isberga. *Icarus*, 248, 516–525.
- Cellino A. and Dell’Oro A. (2012). The derivation of asteroid physical properties from Gaia observations. *Planet. Space Sci.*, 73, 52–55.

- Cellino A., Diolaiti E., Ragazzoni R., et al. (2003). Speckle interferometry observations of asteroids at TNG. *Icarus*, 162, 278–284.
- Cellino A., Hestroffer D., Tanga P., et al. (2009). Genetic inversion of sparse disk-integrated photometric data of asteroids: application to Hipparcos data. *Astron. Astrophys.*, 506, 935–954.
- Cellino A., Tanga P., Dell’Oro A., et al. (2007). Asteroid science with Gaia: Sizes, spin properties, overall shapes and taxonomy. *Advances in Space Research*, 40, 202–208.
- Chapman C. R., Enke B., Merline W. J., et al. (2007). Young Asteroid 832 Karin shows no rotational spectral variations. *Icarus*, 191, 323–329.
- Colas F., Berthier J., Vachier F., et al. (2012). Shape and size of (90) Antiope derived from an exceptional stellar occultation on July 19, 2011. *LPI Contributions*, 1667, 6427.
- Conan J.-M., Fusco T., Mugnier L. M., et al. (2000). MISTRAL: Myopic deconvolution method applied to ADONIS and to simulated VLT-NAOS images. *The Messenger*, 99, 38–45.
- Conrad A. R., Dumas C., Merline W. J., et al. (2007). Direct measurement of the size, shape, and pole of 511 Davida with Keck AO in a single night. *Icarus*, 191, 616–627.
- Delbo M. (2004). The nature of near-Earth asteroids from the study of their thermal infrared emission. *PhD thesis*, pp. 1–210.
- Delbo M. and Harris A. W. (2002). Physical properties of near-Earth asteroids from thermal infrared observations and thermal modeling. *Meteoritics & Planetary Science*, 37, 1929–1936.
- Delbo M., Ligorì S., Matter A., et al. (2009). First VLT-MIDI direct determinations of asteroid sizes. *Astrophys. J.*, 694, 1228–1236.
- Descamps P., Marchis F., Berthier J., et al. (2011). Triplicity and physical characteristics of Asteroid (216) Kleopatra. *Icarus*, 211, 1022–1033.
- Descamps P., Marchis F., Pollock J., et al. (2008). New determination of the size and bulk density of the binary Asteroid 22 Kalliope from observations of mutual eclipses. *Icarus*, 196, 578–600.
- Descamps P., Marchis F., Ďurech J., et al. (2009). New insights on the binary asteroid 121 Hermione. *Icarus*, 203, 88–101.
- Dotto E., Barucci M. A., Müller T. G., et al. (2002). Observations from orbiting platforms. In *Asteroids III* (Bottke W. F., Cellino A., Paolicchi P., et al., editors), pp. 219–234. University of Arizona Press, Tucson.
- Drummond J., Eckart A., and Hege E. K. (1988). Speckle interferometry of asteroids. IV - Reconstructed images of 4 Vesta. *Icarus*, 73, 1–14.
- Drummond J. D., Cocke W. J., Hege E. K., et al. (1985). Speckle interferometry of asteroids. I - 433 Eros. *Icarus*, 61, 132–151.
- Drummond J. D., Conrad A., Merline W., et al. (2009). The dimensions and pole of asteroid (21) Lutetia from adaptive optics images. *AAS/Division for Planetary Sciences Meeting Abstracts*, 41, # 59.07.
- Dunham D. W., Herald D., Frappa E., et al. (2014). Asteroid Occultations V12.0. *NASA Planetary Data System*, 216.
- Ďurech J. and Kaasalainen M. (2003). Photometric signatures of highly nonconvex and binary asteroids. *Astron. Astrophys.*, 404, 709–714.
- Ďurech J., Grav T., Jedicke R., et al. (2005). Asteroid models from the Pan-STARRS photometry. *Earth, Moon, and Planets*, 97, 179–187.
- Ďurech J., Scheirich P., Kaasalainen M., et al. (2007). Physical models of asteroid from sparse photometric data. In *Near Earth Objects, our Celestial Neighbors: Opportunity and Risk* (Milani A., Valsecchi G. B., and Vokrouhlický D., editors), p. 191. Cambridge University Press, Cambridge.
- Ďurech J., Vokrouhlický D., Kaasalainen M., et al. (2008). Detection of the YORP effect in asteroid (1620) Geographos. *Astron. Astrophys.*, 489, L25–L28.
- Ďurech J., Kaasalainen M., Warner B. D., et al. (2009). Asteroid models from combined sparse and dense photometric data. *Astron. Astrophys.*, 493, 291–297.
- Ďurech J., Kaasalainen M., Herald D., et al. (2011). Combining asteroid models derived by lightcurve inversion with asteroidal occultation silhouettes. *Icarus*, 214, 652–670.
- Ďurech J., Delbo M., and Carry B. (2012). Asteroid models derived from thermal infrared data and optical lightcurves. *LPI Contributions*, 1667, 6118.
- Ďurech J., Vokrouhlický D., Baransky A. R., et al. (2012). Analysis of the rotation period of asteroids (1865) Cerberus, (2100) Ra-Shalom, and (3103) Eger – search for the YORP effect. *Astron. Astrophys.*, 547, A10.
- Ďurech J., Hanuš J., Delbo M., et al. (2014). Physical properties of asteroids derived from a novel approach to modeling of optical lightcurves and WISE thermal infrared data. In *AAS/Division for Planetary Sciences Meeting Abstracts*, volume 46 of *AAS/Division for Planetary Sciences Meeting Abstracts*, p. #509.11.
- Eisenhauer F., Perrin G., Brandner W., et al. (2008). GRAVITY: getting to the event horizon of Sgr A\*. In *Society of Photo-Optical Instrumentation Engineers (SPIE) Conference Series*, volume 7013.
- Emery J. P., Cruikshank D. P., and Van Cleve J. (2006). Thermal emission spectroscopy (5.2–38  $\mu\text{m}$ ) of three Trojan asteroids with the Spitzer Space Telescope: Detection of fine-grained silicates. *Icarus*, 182, 496–512.
- Emery J. P., Sprague A. L., Witteborn F. C., et al. (1998). Mercury: Thermal modeling and mid-infrared (5–12  $\mu\text{m}$ ) observations. *Icarus*, 136, 104–123.
- Fang J., Margot J.-L., Brozovic M., et al. (2011). Orbits of near-Earth asteroid triples 2001 SN263 and 1994 CC: Properties, origin, and evolution. *Astron. J.*, 141, 154–169.
- Gaskell R. W., Barnouin-Jha O. S., Scheeres D. J., et al. (2008). Characterizing and navigating small bodies with imaging data. *Meteoritics and Planetary Science*, 43, 1049–1061.
- Golubov O. and Krugly Y. N. (2012). Tangential component of the YORP effect. *Astrophys. J. Lett.*, 752, L11.
- Golubov O., Scheeres D. J., and Krugly Y. N. (2014). A three-dimensional model of tangential YORP. *Astrophys. J.*, 794, 22.
- Grav T., Mainzer A. K., Bauer J., et al. (2012a). WISE/NEOWISE observations of the Hilda population: Preliminary results. *Astrophys. J.*, 744, 197.
- Grav T., Mainzer A. K., Bauer J., et al. (2011). WISE/NEOWISE observations of the Jovian Trojans: Preliminary results. *Astrophys. J.*, 742, 40.
- Grav T., Mainzer A. K., Bauer J. M., et al. (2012b). WISE/NEOWISE observations of the Jovian Trojan population: Taxonomy. *Astrophys. J.*, 759, 49.
- Hanuš J., Delbo M., Ďurech J., et al. (2015). Thermophysical modeling of asteroids from WISE thermal data – Significance of the shape model and the pole orientation uncertainties. *Icarus*, submitted, 0, 0.

- Hanuš J., Marchis F., and Ďurech J. (2013a). Sizes of main-belt asteroids by combining shape models and Keck adaptive optics observations. *Icarus*, 226, 1045–1057.
- Hanuš J., Ďurech J., Brož M., et al. (2013b). Asteroids' physical models from combined dense and sparse photometry and scaling of the YORP effect by the observed obliquity distribution. *Astron. Astrophys.*, 551, A67.
- Hanuš J., Ďurech J., Brož M., et al. (2011). A study of asteroid pole-latitude distribution based on an extended set of shape models derived by the lightcurve inversion method. *Astron. Astrophys.*, 530, A134.
- Harris A. W. (1998). A thermal model for near-Earth asteroids. *Icarus*, 131, 291–301.
- Harris A. W., Fahnestock E. G., and Pravec P. (2009). On the shapes and spins of “rubble pile” asteroids. *Icarus*, 199, 310–318.
- Harris A. W. and Lagerros J. S. V. (2002). Asteroids in the thermal infrared. In *Asteroids III* (Bottke W. F., Cellino A., Paolicchi P., et al., editors), pp. 139–150. University of Arizona Press, Tucson.
- Harris A. W., Pravec P., and Warner B. D. (2012). Looking a gift horse in the mouth: Evaluation of wide-field asteroid photometric surveys. *LPI Contributions*, 1667, 6069.
- Hasegawa S., Müller T. G., Kuroda D., et al. (2013). The asteroid catalog using AKARI IRC slow-scan observations. *PASJ*, 65, 34.
- Henych T. and Pravec P. (2013). Asteroid rotation excitation by subcatastrophic impacts. *Mon. Not. R. Astron. Soc.*, 432, 1623–1631.
- Hestroffer D., Tanga P., Cellino A., et al. (2002). Asteroids observations with the Hubble Space Telescope. I. Observing strategy, and data analysis and modeling process. *Astron. Astrophys.*, 391, 1123–1132.
- Hom E. F. Y., Marchis F., Lee T. K., et al. (2007). AIDA: an adaptive image deconvolution algorithm with application to multi-frame and three-dimensional data. *Journal of the Optical Society of America A*, 24, 1580–1600.
- Hudson R. S., Ostro S. J., and Scheeres D. J. (2003). High-resolution model of Asteroid 4179 Toutatis. *Icarus*, 161, 346–355.
- Jankov S. (2010). Astronomical optical interferometry. I. Methods and instrumentation. *Serbian Astronomical Journal*, 181, 1–17.
- Johansen A. and Lacerda P. (2010). Prograde rotation of protoplanets by accretion of pebbles in a gaseous environment. *Mon. Not. R. Astron. Soc.*, 404, 475–485.
- Jorda L., Lamy P. L., Gaskell R. W., et al. (2012). Asteroid (2867) Steins: Shape, topography and global physical properties from OSIRIS observations. *Icarus*, 221, 1089–1100.
- Kaasalainen M. (2001). Interpretation of lightcurves of precessing asteroids. *Astron. Astrophys.*, 376, 302–309.
- Kaasalainen M. (2004). Physical models of large number of asteroids from calibrated photometry sparse in time. *Astron. Astrophys.*, 422, L39–L42.
- Kaasalainen M. (2011). Maximum compatibility estimates and shape reconstruction with boundary curves and volumes of generalized projections. *Inverse Problems and Imaging*, 5, 37–57.
- Kaasalainen M. and Lamberg L. (2006). Inverse problems of generalized projection operators. *Inverse Problems*, 22, 749–769.
- Kaasalainen M., Mottola S., and Fulchignoni M. (2002a). Asteroid models from disk-integrated data. In *Asteroids III* (Bottke W. F., Cellino A., Paolicchi P., et al., editors), pp. 139–150. University of Arizona Press, Tucson.
- Kaasalainen M. and Nortunen H. (2013). Compact YORP formulation and stability analysis. *Astron. Astrophys.*, 558, A104.
- Kaasalainen M. and Torppa J. (2001). Optimization methods for asteroid lightcurve inversion. I. Shape determination. *Icarus*, 153, 24–36.
- Kaasalainen M., Torppa J., and Muinonen K. (2001). Optimization methods for asteroid lightcurve inversion. II. The complete inverse problem. *Icarus*, 153, 37–51.
- Kaasalainen M., Torppa J., and Piironen J. (2002b). Models of twenty asteroids from photometric data. *Icarus*, 159, 369–395.
- Kaasalainen M., Ďurech J., Warner B. D., et al. (2007). Acceleration of the rotation of asteroid 1862 Apollo by radiation torques. *Nature*, 446, 420–422.
- Kaasalainen M. and Viikinkoski M. (2012). Shape reconstruction of irregular bodies with multiple complementary data sources. *Astron. Astrophys.*, 543, A97.
- Kaasalainen S., Kaasalainen M., and Piironen J. (2005). Ground reference for space remote sensing. Laboratory photometry of an asteroid model. *Astron. Astrophys.*, 440, 1177–1182.
- Keller H. U., Barbieri C., Koschny D., et al. (2010). E-Type asteroid (2867) Steins as imaged by OSIRIS on board Rosetta. *Science*, 327, 190–193.
- Kryszczyńska A., La Spina A., Paolicchi P., et al. (2007). New findings on asteroid spin-vector distributions. *Icarus*, 192, 223–237.
- Lagerros J. S. V. (1996). Thermal physics of asteroids. I. Effects of shape, heat conduction and beaming. *Astron. Astrophys.*, 310, 1011–1020.
- Lagerros J. S. V. (1997). Thermal physics of asteroids. III. Irregular shapes and albedo variegations. *Astron. Astrophys.*, 325, 1226–1236.
- Lagerros J. S. V. (1998). Thermal physics of asteroids. IV. Thermal infrared beaming. *Astron. Astrophys.*, 332, 1123–1132.
- Lamberg L. and Kaasalainen M. (2001). Numerical solution of the Minkowski problem. *J. Comp. Appl. Math.*, 137, 213–227.
- Lebofsky L. A., Sykes M. V., Tedesco E. F., et al. (1986). A refined ‘standard’ thermal model for asteroids based on observations of 1 Ceres and 2 Pallas. *Icarus*, 68, 239–251.
- Li J.-Y., McFadden L. A., Parker J. W., et al. (2006). Photometric analysis of 1 Ceres and surface mapping from HST observations. *Icarus*, 182, 143–160.
- Licandro J., Hargrove K., Kelley M., et al. (2012). 5–14  $\mu\text{m}$  Spitzer spectra of Themis family asteroids. *Astron. Astrophys.*, 537, A73.
- Lowry S. C., Fitzsimmons A., Pravec P., et al. (2007). Direct detection of the asteroidal YORP effect. *Science*, 316, 272–274.
- Lowry S. C., Weissman P. R., Duddy S. R., et al. (2014). The internal structure of asteroid (25143) Itokawa as revealed by detection of YORP spin-up. *Astron. Astrophys.*, 562, A48.
- Mainzer A., Grav T., Bauer J., et al. (2011). NEOWISE Observations of Near-Earth Objects: Preliminary Results. *Astrophys. J.*, 743, 156.
- Mainzer A., Grav T., Masiero J., et al. (2012a). Physical parameters of asteroids estimated from the WISE 3-band data and NEOWISE post-cryogenic survey. *Astrophys. J. Lett.*, 760, L12.
- Mainzer A., Grav T., Masiero J., et al. (2012b). Characterizing subpopulations within the near-Earth objects with NEOWISE: Preliminary results. *Astrophys. J.*, 752, 110.
- Marchis F., Ďurech J., Castillo-Rogez J., et al. (2014). The puzzling mutual orbit of the binary Trojan asteroid (624) Hektor. *Astrophys. J. Lett.*, 783, L37.

- Marchis F., Kaasalainen M., Hom E. F. Y., et al. (2006). Shape, size and multiplicity of main-belt asteroids. *Icarus*, 185, 39–63.
- Marchis F., Vachier F., Ďurech J., et al. (2013). Characteristics and large bulk density of the C-type main-belt triple asteroid (93) Minerva. *Icarus*, 224, 178–191.
- Masiero J., Jedicke R., Ďurech J., et al. (2009). The thousand asteroid light curve survey. *Icarus*, 204, 145–171.
- Masiero J. R., Mainzer A. K., Grav T., et al. (2011). Main belt asteroids with WISE/NEOWISE. I. Preliminary albedos and diameters. *Astrophys. J.*, 741, 68.
- Masiero J. R., Mainzer A. K., Grav T., et al. (2012). Preliminary analysis of WISE/NEOWISE 3-band cryogenic and post-cryogenic observations of main belt asteroids. *Astrophys. J. Lett.*, 759, L8.
- Matter A., Delbo M., Carry B., et al. (2013). Evidence of a metal-rich surface for the asteroid (16) Psyche from interferometric observations in the thermal infrared. *Icarus*, 226, 419–427.
- Matter A., Delbo M., Ligorì S., et al. (2011). Determination of physical properties of the asteroid (41) Daphne from interferometric observations in the thermal infrared. *Icarus*, 215, 47–56.
- Merline W. J., Drummond J. D., Carry B., et al. (2013). The Resolved Asteroid Program - Size, shape, and pole of (52) Europa. *Icarus*, 225, 794–805.
- Mignard F., Cellino A., Muinonen K., et al. (2007). The Gaia mission: Expected applications to asteroid science. *Earth Moon and Planets*, 101, 97–125.
- Miller J. K., Konopliv A. S., Antreasian P. G., et al. (2002). Determination of shape, gravity, and rotational state of asteroid 433 Eros. *Icarus*, 155, 3–17.
- Millis R. L. and Dunham D. W. (1989). Precise measurement of asteroid sizes and shapes from occultations. In *Asteroids II* (Binzel R. P., Gehrels T., and Matthews M. S., editors), pp. 148–170.
- Mommert M., Farnocchia D., Hora J. L., et al. (2014). Physical properties of near-Earth asteroid 2011 MD. *Astrophys. J. Lett.*, 789, L22.
- Mueller M. (2007). Surface properties of asteroids from mid-infrared observations and thermophysical modeling. *PhD thesis on arXiv.org*, p. 3993.
- Mugnier L. M., Fusco T., and Conan J.-M. (2004). MISTRAL: a myopic edge-preserving image restoration method, with application to astronomical adaptive-optics-corrected long-exposure images. *Journal of the Optical Society of America A*, 21, 1841–1854.
- Müller T. G., Lellouch E., Stansberry J., et al. (2010). “TNOs are Cool”: A survey of the trans-Neptunian region. I. Results from the Herschel science demonstration phase (SDP). *Astron. Astrophys.*, 518, L146.
- Naidu S. P., Margot J.-L., Busch M. W., et al. (2013). Radar imaging and physical characterization of near-Earth Asteroid (162421) 2000 ET70. *Icarus*, 226, 323–335.
- Nathues A., Mottola S., Kaasalainen M., et al. (2005). Spectral study of the Eunomia asteroid family. I. Eunomia. *Icarus*, 175, 452–463.
- Nelan E. P., Lupie O. L., McArthur B., et al. (1998). Fine guidance sensors aboard the Hubble Space Telescope: the scientific capabilities of these interferometers. In *Astronomical Interferometry* (Reasenberg R. D., editor), volume 3350 of *Society of Photo-Optical Instrumentation Engineers (SPIE) Conference Series*, pp. 237–247.
- Ostro S. J., Hudson R. S., Nolan M. C., et al. (2000). Radar observations of asteroid 216 Kleopatra. *Science*, 288, 836–839.
- Ostro S. J., Margot J.-L., Benner L. A. M., et al. (2006). Radar imaging of binary near-Earth asteroid (66391) 1999 KW4. *Science*, 314, 1276–1280.
- Ostro S. J., Rosema K. D., Campbell D. B., et al. (2002). Note: Radar observations of asteroid 1862 Apollo. *Icarus*, 156, 580–583.
- Polishook D., Ofek E. O., Waszczak A., et al. (2012). Asteroid rotation periods from the Palomar Transient Factory survey. *Mon. Not. R. Astron. Soc.*, 421, 2094–2108.
- Pravec P., Harris A. W., Vokrouhlický D., et al. (2008). Spin rate distribution of small asteroids. *Icarus*, 197, 497–504.
- Pravec P., Scheirich P., Kušnirák P., et al. (2006). Photometric survey of binary near-Earth asteroids. *Icarus*, 181, 63–93.
- Pravec P., Scheirich P., Ďurech J., et al. (2014). The tumbling spin state of (99942) Apophis. *Icarus*, 233, 48–60.
- Pravec P., Vokrouhlický D., Polishook D., et al. (2010). Formation of asteroid pairs by rotational fission. *Nature*, 466, 1085–1088.
- Preusker F., Scholten F., Knollenberg J., et al. (2012). The northern hemisphere of asteroid (21) Lutetia – topography and orthoimages from Rosetta OSIRIS NAC image data. *Planet. Space Sci.*, 66, 54–63.
- Pursiainen S. and Kaasalainen M. (2013). Iterative alternating sequential (IAS) method for radio tomography of asteroids in 3D. *Planet. Space Sci.*, 82, 84–98.
- Pursiainen S. and Kaasalainen M. (2014a). Detection of anomalies in radio tomography of asteroids: Source count and forward errors. *Planet. Space Sci.*, 99, 36–37.
- Pursiainen S. and Kaasalainen M. (2014b). Sparse source travel-time tomography of a laboratory target: accuracy and robustness of anomaly detection. *Inverse Problems*, 30, 114016.
- Ragazzoni R., Baruffolo A., Marchetti E., et al. (2000). Speckle interferometry measurements of the asteroids 10-Hygiea and 15-Eunomia. *Astron. Astrophys.*, 354, 315–320.
- Rozitis B. and Green S. F. (2011). Directional characteristics of thermal-infrared beaming from atmosphereless planetary surfaces - a new thermophysical model. *Mon. Not. R. Astron. Soc.*, 415, 2042–2062.
- Russell C. T., Raymond C. A., Coradini A., et al. (2012). Dawn at Vesta: Testing the protoplanetary paradigm. *Science*, 336, 684–686.
- Russell H. N. (1906). On the light variations of asteroids and satellites. *Astrophys. J.*, 24, 1–18.
- Sasaki T., Sasaki S., Watanabe J.-i., et al. (2004). Mature and fresh surfaces on the newborn asteroid Karin. *Astrophys. J.*, 615, L161–L164.
- Scheirich P., Ďurech J., Pravec P., et al. (2010). The shape and rotation of asteroid 2008 TC<sub>3</sub>. *Meteoritics and Planetary Science*, 45, 1804–1811.
- Scheirich P. and Pravec P. (2009). Modeling of lightcurves of binary asteroids. *Icarus*, 200, 531–547.
- Schmidt B. E., Thomas P. C., Bauer J. M., et al. (2009). The shape and surface variation of 2 Pallas from the Hubble Space Telescope. *Science*, 326, 275–278.
- Ševeček P., Brož M., Čapek D., et al. (2015). The thermal emission from boulders on (25143) Itokawa and general implications for the YORP effect. *Mon. Not. R. Astron. Soc.*, submitted, 0, 0–0.
- Shepard M. K., Margot J.-L., Magri C., et al. (2006). Radar and infrared observations of binary near-Earth Asteroid 2002 CE26. *Icarus*, 184, 198–210.

- Sicardy B., Ortiz J. L., Assafin M., et al. (2011). A Pluto-like radius and a high albedo for the dwarf planet Eris from an occultation. *Nature*, 478, 493–496.
- Sierks H., Lamy P., Barbieri C., et al. (2011). Images of asteroid 21 Lutetia: A remnant planetesimal from the early solar system. *Science*, 334, 487–490.
- Spencer J. R. (1990). A rough-surface thermophysical model for airless planets. *Icarus*, 83, 27–38.
- Spencer J. R., Lebofsky L. A., and Sykes M. V. (1989). Systematic biases in radiometric diameter determinations. *Icarus*, 78, 337–354.
- Statler T. S. (2009). Extreme sensitivity of the YORP effect to small-scale topography. *Icarus*, 202, 502–513.
- Szabó G. M. and Kiss L. L. (2008). The shape distribution of asteroid families: Evidence for evolution driven by small impacts. *Icarus*, 196, 135–143.
- Takahashi Y. and Scheeres D. J. (2014). Morphology driven density distribution estimation for small bodies. *Icarus*, 233, 179–193.
- Tanga P. and Delbo M. (2007). Asteroid occultations today and tomorrow: toward the GAIA era. *Astron. Astrophys.*, 474, 1015–1022.
- Tanga P., Hestroffer D., Berthier J., et al. (2001). NOTE: HST/FGS Observations of the Asteroid (216) Kleopatra. *Icarus*, 153, 451–454.
- Tanga P., Hestroffer D., Cellino A., et al. (2003). Asteroid observations with the Hubble Space Telescope. II. Duplicity search and size measurements for 6 asteroids. *Astronomy and Astrophysics*, 401, 733–741.
- Tedesco E. F., Noah P. V., Noah M., et al. (2002). The Supplemental IRAS Minor Planet Survey. *The Astronomical Journal*, 123, 1056–1085.
- Thomas P. C., Binzel R. P., Gaffey M. J., et al. (1997). Impact excavation on asteroid 4 Vesta: Hubble Space Telescope results. *Science*, 277, 1492–1495.
- Thomas P. C., Parker J. W., McFadden L. A., et al. (2005). Differentiation of the asteroid Ceres as revealed by its shape. *Nature*, 437, 224–226.
- Timerson B., Āurech J., Aguirre S., et al. (2009). A trio of well-observed asteroid occultations in 2008. *Minor Planet Bulletin*, 36, 98–100.
- Torppa J., Kaasalainen M., Michalowski T., et al. (2003). Shapes and rotational properties of thirty asteroids from photometric data. *Icarus*, 164, 346–383.
- Trilling D. E., Mueller M., Hora J. L., et al. (2010). Explore-NEOs. I. Description and first results from the warm Spitzer near-Earth object survey. *Astron. J.*, 140, 770–784.
- Usui F., Kasuga T., Hasegawa S., et al. (2013). Albedo properties of main belt asteroids based on the all-sky survey of the infrared astronomical satellite AKARI. *Astrophys. J.*, 762, 56.
- Usui F., Kuroda D., Müller T. G., et al. (2011). Asteroid catalog using Akari: AKARI/IRC mid-infrared asteroid survey. *PASJ*, 63, 1117–1138.
- Vachier F., Berthier J., and Marchis F. (2012). Determination of binary asteroid orbits with a genetic-based algorithm. *Astron. Astrophys.*, 543, A68.
- Vernazza P., Rossi A., Birlan M., et al. (2007). 832 Karin: Absence of rotational spectral variations. *Icarus*, 191, 330–336.
- Viikinkoski M. and Kaasalainen M. (2014). Shape reconstruction from images: Pixel fields and Fourier transform. *Inverse Problems and Imaging*, 8, 885–900.
- Viikinkoski M., Kaasalainen M., and Āurech J. (2015). ADAM: a general method of including any data types in asteroid reconstruction. *Astron. Astrophys.*, submitted, 0, 0.
- Walsh K. J., Richardson D. C., and Michel P. (2008). Rotational breakup as the origin of small binary asteroids. *Nature*, 454, 188–191.
- Warner B. D., Harris A. W., and Pravec P. (2009). The asteroid lightcurve database. *Icarus*, 202, 134–146.
- Warner B. D., Stephens R. D., and Harris A. W. (2011). Save the lightcurves. *Minor Planet Bulletin*, 38, 172–174.
- Witasse O., Lebreton J.-P., Bird M. K., et al. (2006). Overview of the coordinated ground-based observations of Titan during the Huygens mission. *Journal of Geophysical Research (Planets)*, 111, 7–19.
- Zou X., Li C., Liu J., et al. (2014). The preliminary analysis of the 4179 Toutatis snapshots of the Chang’E-2 flyby. *Icarus*, 229, 348–354.